arXiv:1511.05576v1 [astro-ph.GA] 17 Nov 2015

Spectroscopy of Luminous Compact Blue Galaxies in Distant Clusters II. Physical Properties of dE Progenitor Candidates

S. M. Crawford[1], Gregory D. Wirth[2], M. A. Bershady,[3]and S. M. Randriamampandry[4]

ABSTRACT

Luminous Compact Blue Galaxies (LCBGs) are an extreme star-bursting population of galaxies that were far more common at earlier epochs than today. Based on spectroscopic and photometric measurements of LCBGs in massive ($M > 10^{15} M_{\odot}$), intermediate redshift ($0.5 < z < 0.9$) galaxy clusters, we present their rest-frame properties including star-formation rate, dynamical mass, size, luminosity, and metallicity. The appearance of these small, compact galaxies in clusters at intermediate redshift helps explain the observed redshift evolution in the size-luminosity relationship among cluster galaxies. In addition, we find the rest-frame properties of LCBGs appearing in galaxy clusters are indistinguishable from field LCBGs at the same redshift. Up to 35% of the LCBGs show significant discrepancies between optical and infrared indicators of star formation, suggesting that star formation occurs in obscured regions. Nonetheless, the star formation for LCBGs shows a decrease toward the center of the galaxy clusters. Based on their position and velocity, we estimate that up to 10% of cluster LCBGs are likely to merge with another cluster galaxy. Finally, the observed properties and distributions of the LCBGs in these clusters lead us to conclude that we are witnessing the quenching of the progenitors of dwarf elliptical galaxies that dominate the number density of present-epoch galaxy clusters.

Subject headings: galaxies:clusters: general — galaxies: evolution

[1]South African Astronomical Observatory, Observatory, 7935 Cape Town, South Africa; crawford@saao.ac.za

[2]W. M. Keck Observatory, 65-1120 Mamalahoa Hwy, Kamuela HI 96743; gregory.wirth@gmail.com

[3]Washburn Observatories, U. Wisconsin - Madison, 475 N. Charter St., Madison, WI 53706; mab@astro.wisc.edu

[4]Astrophysics & Cosmology Research Unit, School of Mathematics, Statistics & Computer Science, University of KwaZulu-Natal, Durban 4041, South Africa

1. Introduction

Luminous Compact Blue Galaxies (LCBGs) are an extreme, star-bursting population of galaxies (Koo et al. 1994) found both within clusters of galaxies (Koo et al. 1997; Crawford et al. 2006) and outside. The number density and star-formation rate of LCBGs have decreased over time in concert with the global star formation rate (Guzmán et al. 1997). However, beyond having high surface brightness and blue colors, field LCBGs are heterogeneous in their morphologies: some objects are extremely compact, some appear to be undergoing nuclear starbursts, and others display very irregular morphologies (Guzman et al. 1996; Phillips et al. 1997; Kobulnicky & Zaritsky 1999; Guzmán et al. 2003; Garland et al. 2004; Werk et al. 2004; Barton et al. 2006; Noeske et al. 2006; Rawat et al. 2007; Hoyos et al. 2007; Tollerud et al. 2010). This heterogenous nature has led researchers to propose a variety of evolutionary outcomes for LCBGs, including evolving into low-luminosity spheroidal systems (Koo et al. 1994; Guzman et al. 1996) and the bulges of spiral galaxies (Barton & van Zee 2001; Hammer et al. 2001).

The dramatic increase in the fraction of blue galaxies (Butcher & Oemler 1984) in clusters at high redshift tracks the increase in star-forming galaxies in the field (Ellis 1997). Due to a variety of cluster processes (Boselli & Gavazzi 2006), the blue galaxies in clusters are likely to have their star formation quenched, and if they are falling into the cluster for the first time, they will experience significant stripping of both their gas and stellar material. For this reason, star-forming galaxies in clusters have long been proposed as the possible progenitors of dwarf elliptical galaxies (Couch et al. 1994; Moore et al. 1998; Tran et al. 2005).

Other than very early work by Koo et al. (1997) confirming their presence in clusters, relatively few studies have targeted the cluster LCBG population; however, recent observations have indicated that the cluster environment is triggering the LCBG phase (Crawford et al. 2006, 2011). In fact, their kinematic and spatial distributions suggest that LCBGs represent galaxies experiencing initial infall into galaxy clusters (Crawford et al. 2014).

In this work, we characterize the properties of LCBGs in galaxy clusters in order to assess how they might evolve over time. In §2, we briefly summarize the observational data underlying this work. A description of the different techniques used to derive the rest-frame properties of our sample follows in §3. We present various properties of LCBGs and compare them to other populations in §4. Finally, in §5, we present possible fates for LCBGs in galaxy clusters. Throughout this work, we adopt $H_0 = 70$ km s^{-1} Mpc^{-1}, $\Omega_M = 0.3$, and $\Omega_\Lambda = 0.7$.

1.1. Definition of Galaxy Classifications

Following Crawford et al. (2011, 2014), we use the following definitions for our different samples discussed in this paper to divide the galaxy populations into three samples based on their color and compactness:

- Red Sequence (RS) are defined as objects redder than the dividing line between blue and red objects, which we define as $U - B = -0.032 \times (M_B + 21.52) + 0.204$ following Willmer et al. (2006)
- Blue cloud (BC) galaxies are defined as objects bluer than the dividing line between blue and red objects, which we define as $U - B = -0.032 \times (M_B + 21.52) + 0.204$ following Willmer et al. (2006)
- Luminous compact blue galaxies (LCBGs) are a subset of the BC class, defined as having $B - V < 0.5$, $\mu_B < 21$ mag arcsec^{-2}, and $M_B < -18.5$ (Garland et al. 2004; Crawford et al. 2006).

Throughout this work, we compare our results to the field sample produced by Guzmán et al. (1997). Their definition of compact objects is in apparent properties, but once transformed into absolute space, it is very similar to the definition for LCBGs that we use here.

2. Observations

Full details of the observations are presented in our previous works (Crawford et al. 2006, 2011, 2014), but here we present a brief description of our sample selection and observations. The set of galaxy clusters used in our work are summarized in Table 1. We originally selected this set of clusters based on their extreme richness, their intermediate redshifts, and their large existing set of archive data. We identified LCBGs through their photometric properties from deep imaging on the WIYN telescope for spectroscopic follow-up with the Deep Imaging Multi-Object Spectrograph (DEIMOS) on the Keck Telescope. Based on their spectroscopic redshifts, LCBGs were identified as being either part of the cluster or in the field (Crawford et al. 2014). In total, we have 381 LCBGs with spectroscopic redshifts in our sample. Of those, 119 are cluster LCBGs and 262 are field LCBGs. Of the cluster (field) LCBGs, we have DEIMOS spectra for 53 (80) galaxies and all of those galaxies have [O II] λ3727 detections. Of that sample, 33 (41) cluster (field) LCBGs have Hubble Space Telescope (HST) imaging and 18 (19) cluster (field) LCBGs have far-infrared measurements from the Spitzer Space Telescope.

Table 1. Summary of Cluster Observations

Cluster	α (J2000)	δ (J2000)	z	σ_p (km s^{-1})	Hubble Space Telescope				Spitzer Space Telescope		
					PropID	Instrument	ExpTime s	Filter	ExpTime s	RMS μJy	SEIP Data Tag ADS/IRSA.Atlas/
MS 0451-03	04:54:10.8	−03:00:51	0.5389	1328 ± 47	9836	ACS	2036	F814W	1637	26	#2013/0325/072424_12320
Cl 0016+16	00:18:33.6	+16:26:16	0.5467	1490 ± 80	6825	WFPC2	4600	F814W	764	28	#2015/0309/051809_29746
					10493	ACS	2183	F775W			
Cl J1324+3011	13:24:48.8	+30:11:39	0.7549	806 ± 85							
MS 1054-03	10:56:60.0	−03:37:36	0.8307	1105 ± 61	9772	ACS	1980	F814W	3218	19	#2015/0309/052253_30941
					10196	ACS	2160	F814W			
Cl J1604+4304	16:04:24.0	+43:04:39	0.9005	1106 ± 167	10496	ACS	1500	F850LP	1389	13	#2015/0309/053231_935

Note. — (1) Cluster Field of the Observationts (2) and (3) celestial coordinates of the adopted cluster center defined by Brightest Cluster Galaxy; (4) measured cluster redshift; (5) measured cluster projected velocity dispersion (6) HST Proposal ID (7) HST Instrument (8) Typical Exposure Time (9) Filter (10) Mean Exposure Time (11) RMS Noise (12) Spitzer Enhanced Image Product ID

2.1. WIYN Imaging

Deep imaging data in UBRIz and two narrow bands were obtained with the Mini-Mosaic camera from the WIYN 3.5 m telescope for all five clusters between 1999 October and 2004 June. The Mini-Mosaic camera has a $9\farcm6 \times 9\farcm6$ FOV with $0\farcs14$ px^{-1} plate scale. In the R band, the median value for the seeing was FWHM=$0\farcs85$. The narrow-band filters were specifically designed to detect [O II] λ3727 at the redshift of each cluster. Details of the data reduction and analysis appear in Crawford et al. (2009).

2.2. Spectroscopic Observations

We obtained spectroscopic observations for a sample of cluster star-forming galaxies with the Deep Imaging Multi-Object Spectrograph (DEIMOS, Faber et al. 2003) on the Keck II Telescope during October 2005 and April 2007. Different instrument configurations were used in order to sample key diagnostic features at the redshift of each cluster. Full details of the observations and data reductions are given in Crawford et al. (2011).

2.3. HST Imaging

All of the clusters have been the target of extensive observations with the Hubble Space Telescope (HST), primarily using either WFPC2 or the Adva nced Camera for Surveys (ACS). WFPC2 has a chevron-shaped field of view over $2\farcm5 \times 2\farcm5$ region with a pixel scale of $0\farcs1$ px^{-1} (McMaster et al. 2008). The ACS camera has a field of view of $3\farcm7 \times 3\farcm7$ with a pixel scale of $0\farcs05$ px^{-1} (Ubeda et al. 2014). For all measurements, we have attempted to select data taken in a filter closest to the rest-frame B band. We have employed ACS imaging data whenever possible and substituted WFPC2 images only when required. In Table 1, we summarize all of the HST observations that are used in this work.

2.4. Spitzer Observations

For clusters observed in the far-infrared regime by the Spitzer Space Telescope, we extracted MIPS 24 μm flux densities, S_{24}, from images obtained through the Enhanced Imaging Products[5] archive following the procedures outlined in Randriamampandry et al.

[5] `http://irsa.ipac.caltech.edu/data/SPITZER/Enhanced/SEIP/`

(2015). In Table 1, we list the details of each of these observations.

3. Data Analysis

In this section, we describe the different methods we used to determine the properties of the galaxies, including measuring their photometry, size, rest-frame properties, and spectroscopic properties. In Table 3, we report on the properties of these sources.

Table 2. Measured Properties of LCBGs

Object (1)	α (J2000) (2)	β (J2000) (3)	z (4)	M_B (mag) (5)	r_e (kpc) (6)	σ ($km\ s^{-1}$) (7)	Mass ($10^9\ M_\odot$) (8)	SFR(OII) ($M_\odot\ yr^{-1}$) (9)	SFR(IR) ($M_\odot\ yr^{-1}$) (10)	12+log(O/H) (dex) (11)
					Cluster LCBG					
WLTV J001828.43+162615.7	4.6184760	16.4377106	0.5442	-18.57 ± 0.05	3.33 ± 1.65^H	26 ± 3	2.5 ± 1.3	0.54 ± 0.2	...	8.7 ± 0.8
WLTV J001829.15+162653.4	4.6214648	16.4481822	0.5378	-19.65 ± 0.04	1.89 ± 0.29^H	90 ± 5	17.4 ± 2.8	0.97 ± 0.1	14.09 ± 0.4	7.8 ± 0.4
WLTV J001831.90+162441.1	4.6329173	16.4114185	0.5464	-19.99 ± 0.04	2.27 ± 0.38^H	59 ± 9	9.0 ± 2.1	0.35 ± 0.0	...	...
WLTV J001834.81+162719.9	4.6450259	16.4555305	0.5392	-20.12 ± 0.04	2.65 ± 0.64^W	68 ± 13	13.9 ± 4.4	3.26 ± 0.3	4.68 ± 0.9	8.4 ± 0.4
WLTV J001836.15+162635.5	4.6506133	16.4431949	0.5469	-20.26 ± 0.04	1.29 ± 0.65^W	44 ± 9	2.8 ± 1.6	0.83 ± 0.1	...	8.9 ± 0.3
WLTV J001836.69+162645.6	4.6528944	16.4460093	0.5571	-19.35 ± 0.05	2.63 ± 0.88^H	110 ± 12	36.2 ± 12.7	0.59 ± 0.1	...	9.0 ± 0.4
WLTV J001839.47+162414.2	4.6644431	16.4039527	0.5559	-20.19 ± 0.05	1.30 ± 0.65^W	45 ± 2	3.0 ± 1.5	2.91 ± 0.8	...	9.0 ± 0.5
WLTV J001838.51+162513.7	4.6604379	16.4204798	0.5371	-19.77 ± 0.04	2.58 ± 0.51^H	49 ± 13	7.0 ± 2.3	0.72 ± 0.1	...	8.4 ± 0.3
WLTV J001841.98+162524.8	4.6749359	16.4235667	0.5573	-20.04 ± 0.06	1.90 ± 0.21^H	23 ± 2	1.1 ± 0.2	1.66 ± 0.7	...	8.9 ± 1.0
WLTV J001843.56+162606.0	4.6815191	16.4350089	0.5541	-20.57 ± 0.04	3.34 ± 0.01^H	48 ± 2	8.9 ± 0.5	1.17 ± 0.0	...	9.0 ± 0.1
WLTV J001845.83+162643.3	4.6909432	16.4453646	0.5393	-21.21 ± 0.03	1.75 ± 0.03^H	50 ± 4	5.0 ± 0.5	4.70 ± 0.1	15.53 ± 0.4	8.8 ± 0.0
WLTV J001845.90+162748.4	4.6912518	16.4634667	0.5394	-19.46 ± 0.04	1.60 ± 0.65^H	36 ± 14	2.4 ± 1.3	1.78 ± 0.3	...	8.4 ± 0.6
WLTV J001847.60+162614.8	4.6983474	16.4374512	0.5528	-20.14 ± 0.04	2.14 ± 0.65^W	32 ± 2	2.6 ± 0.8	1.05 ± 0.2	11.34 ± 0.5	9.0 ± 0.3
WLTV J045358.78-025857.2	73.4949225	-2.9825687	0.5381	-20.83 ± 0.04	3.82 ± 1.08^H	26 ± 2	3.0 ± 0.9	1.38 ± 0.2	...	...
WLTV J045401.42-030125.6	73.5059232	-3.0238011	0.5401	-20.10 ± 0.04	2.10 ± 0.18^H	37 ± 3	3.4 ± 0.5	2.88 ± 0.2	6.88 ± 0.6	8.5 ± 0.2
WLTV J045401.78-030054.4	73.5074178	-3.0151296	0.5321	-20.19 ± 0.04	2.78 ± 0.02^H	66 ± 7	13.8 ± 1.6	2.71 ± 0.2	10.11 ± 0.4	8.6 ± 0.1
WLTV J045401.86-030029.2	73.5077568	-3.0081267	0.5114	-20.86 ± 0.03	1.31 ± 0.03^H	53 ± 3	4.2 ± 0.3	5.26 ± 0.1	6.71 ± 0.6	8.7 ± 0.0
WLTV J045403.40-025920.3	73.5141490	-2.9889974	0.5315	-19.74 ± 0.04	2.33 ± 0.47^H	72 ± 8	13.8 ± 3.2	1.42 ± 0.3	20.51 ± 0.2	8.7 ± 0.3
WLTV J045405.10-025939.1	73.5212652	-2.9942039	0.5271	-22.13 ± 0.03	6.84 ± 0.18^H	49 ± 3	18.4 ± 1.3	1.53 ± 0.5	23.35 ± 0.2	...
WLTV J045405.56-025918.3	73.5231756	-2.9884231	0.5300	-22.03 ± 0.04	6.73 ± 0.23^H	184 ± 5	255.1 ± 12.1	3.40 ± 0.1	17.61 ± 0.3	8.7 ± 0.0
WLTV J045405.27-025950.0	73.5219589	-2.9972233	0.5388	-20.35 ± 0.04	2.40 ± 0.12^H	74 ± 26	14.8 ± 5.3	1.26 ± 0.1	...	8.7 ± 0.1
WLTV J045406.22-030020.3	73.5259274	-3.0056456	0.5311	-19.03 ± 0.04	1.63 ± 0.04^H	50 ± 24	4.6 ± 2.2	0.97 ± 0.2	...	8.6 ± 0.4
WLTV J045411.85-030407.7	73.5493753	-3.0688174	0.5292	-20.24 ± 0.04	3.08 ± 0.23^H	108 ± 8	40.8 ± 4.4	0.30 ± 0.0	14.78 ± 0.4	...
WLTV J045412.07-030201.2	73.5502925	-3.0336742	0.5285	-19.77 ± 0.04	2.36 ± 0.36^H	42 ± 3	4.7 ± 0.8	1.27 ± 0.1	...	7.9 ± 0.3
WLTV J045411.58-025630.4	73.5482314	-2.9417774	0.5470	-18.98 ± 0.06	2.52 ± 0.95^H	26 ± 2	2.0 ± 0.8	1.97 ± 1.5	...	...
WLTV J045412.68-030054.2	73.5528434	-3.0150628	0.5443	-20.75 ± 0.04	1.87 ± 0.10^H	47 ± 28	4.8 ± 2.8	0.84 ± 0.0	15.09 ± 0.3	8.9 ± 0.1
WLTV J045413.51-030148.4	73.5562996	-3.0301159	0.5478	-20.19 ± 0.04	3.12 ± 0.41^H	77 ± 28	20.7 ± 8.0	1.35 ± 0.1	4.24 ± 0.8	8.9 ± 0.1
WLTV J045414.98-030424.4	73.5624305	-3.0734561	0.5299	-20.30 ± 0.04	3.40 ± 0.33^H	80 ± 4	24.7 ± 2.8	1.53 ± 0.1	...	8.5 ± 0.2
WLTV J045415.18-030331.9	73.5632546	-3.0588815	0.5351	-20.04 ± 0.04	1.85 ± 0.16^H	44 ± 2	4.2 ± 0.4	2.66 ± 0.2	...	8.6 ± 0.2
WLTV J045421.25-030325.9	73.5885575	-3.0571959	0.5420	-19.38 ± 0.04	2.26 ± 0.36^H	< 10	0.2 ± 0.1	0.75 ± 0.1	...	8.1 ± 0.6
WLTV J045421.31-030230.0	73.5888003	-3.0416920	0.5109	-18.64 ± 0.05	2.29 ± 0.55^H	45 ± 4	5.2 ± 1.4	0.51 ± 0.1	...	8.7 ± 0.5
WLTV J045424.11-030348.0	73.6004433	-3.0633382	0.5062	-19.92 ± 0.04	2.08 ± 0.12^H	62 ± 7	9.2 ± 1.2	1.05 ± 1.0	...	8.0 ± 1.3
WLTV J105655.78-033544.2	164.2324078	-3.5956237	0.8244	-18.88 ± 0.04	0.91 ± 0.08^H	69 ± 4	4.9 ± 0.5	0.90 ± 0.4	...	...
WLTV J105706.06-033603.6	164.2752425	-3.6010122	0.8293	-19.54 ± 0.06	2.17 ± 0.42^H	< 10	0.2 ± 0.0	1.06 ± 0.5	3.32 ± 0.7	...
WLTV J105712.03-034135.3	164.3001342	-3.6931475	0.8319	-18.56 ± 0.07	1.67 ± 0.77^W	44 ± 15	3.7 ± 2.2	0.40 ± 0.4	...	...
WLTV J105653.85-033402.1	164.2243902	-3.5672541	0.8305	-20.72 ± 0.05	2.17 ± 0.42^H	29 ± 12	2.2 ± 1.0	...	...	...
WLTV J132445.28+301031.0	201.1886774	30.1752830	0.7529	-19.81 ± 0.06	3.54 ± 0.74^W	148 ± 7	87.5 ± 18.9	0.92 ± 0.1	...	8.8 ± 0.3
WLTV J132448.33+300748.5	201.2013649	30.1301409	0.7613	-20.90 ± 0.04	4.98 ± 0.75^W	91 ± 8	46.1 ± 8.2	0.80 ± 0.2	...	9.1 ± 0.4
WLTV J132526.34+300926.7	201.3597635	30.1574307	0.7530	-20.17 ± 0.05	2.74 ± 0.74^W	136 ± 5	56.6 ± 15.5	1.41 ± 0.1	...	8.9 ± 0.4
WLTV J132527.34+301002.5	201.3639153	30.1673657	0.7414	-20.17 ± 0.05	3.88 ± 0.74^W	140 ± 29	86.0 ± 24.3	0.69 ± 0.1	...	...
WLTV J132531.77+301119.8	201.3823760	30.1888353	0.7417	-20.15 ± 0.04	3.51 ± 0.74^W	50 ± 3	10.1 ± 2.3	1.85 ± 0.2	...	8.8 ± 1.3
WLTV J160407.17+430444.2	241.0298930	43.0789545	0.9010	-22.54 ± 0.09	4.91 ± 0.79^W	120 ± 15	80.1 ± 16.6	5.05 ± 0.6	...	9.2 ± 0.7
WLTV J160410.04+430400.6	241.0418319	43.0668580	0.9085	-20.58 ± 0.05	5.10 ± 0.79^W	55 ± 7	17.2 ± 3.5	4.56 ± 1.0	...	...
WLTV J160410.74+430420.5	241.0447607	43.0723872	0.9083	-21.61 ± 0.04	7.27 ± 0.79^W	37 ± 3	11.3 ± 1.7	4.17 ± 0.3	3.90 ± 0.4	8.8 ± 1.2
WLTV J160418.72+430720.8	241.0779907	43.1224440	0.9047	-18.92 ± 0.08	2.11 ± 0.79^W	64 ± 92	9.7 ± 14.4	0.84 ± 0.2	...	...
WLTV J160418.99+430331.9	241.0791221	43.0588682	0.8820	-21.12 ± 0.08	1.65 ± 0.85^H	190 ± 49	67.0 ± 38.7	2.92 ± 0.4	24.25 ± 0.1	8.9 ± 0.4
WLTV J160423.09+430208.8	241.0962242	43.0357862	0.8944	-21.30 ± 0.05	6.17 ± 0.79^W	83 ± 7	48.2 ± 7.6	8.80 ± 0.8	0.77 ± 0.9	8.3 ± 1.5

Table 2—Continued

Object (1)	α (J2000) (2)	β (J2000) (3)	z (4)	M_B (mag) (5)	r_e (kpc) (6)	σ ($km\ s^{-1}$) (7)	Mass ($10^9\ M_\odot$) (8)	SFR(OII) ($M_\odot\ yr^{-1}$) (9)	SFR(IR) ($M_\odot\ yr^{-1}$) (10)	12+log(O/H) (dex) (11)
WLTV J160425.18+430416.8	241.1049144	43.0713390	0.9010	-21.29 ± 0.04	5.34 ± 2.50^H	42 ± 5	11.0 ± 5.3	2.97 ± 0.3	9.27 ± 0.2	9.2 ± 0.2
WLTV J160447.47+430757.4	241.1977973	43.1326179	0.9037	-20.38 ± 0.07	2.93 ± 0.79^W	47 ± 5	7.2 ± 2.2	3.89 ± 0.5	...	6.7 ± 0.4
WLTV J160447.88+430805.8	241.1994986	43.1349592	0.9023	-22.07 ± 0.04	3.50 ± 0.79^W	64 ± 6	16.1 ± 3.9	16.47 ± 0.6	...	7.0 ± 0.3
Field LCBG										
WLTV J001814.36+162511.0	4.5598337	16.4197472	0.6556	-21.33 ± 0.04	5.66 ± 0.70^W	91 ± 6	52.5 ± 7.5	2.31 ± 0.1	27.16 ± 0.3	9.0 ± 0.1
WLTV J001824.52+162713.9	4.6021678	16.4538719	0.5825	-20.48 ± 0.04	1.79 ± 0.13^H	73 ± 4	10.7 ± 1.0	1.44 ± 0.2	8.91 ± 0.5	9.0 ± 0.2
WLTV J001827.44+162606.7	4.6143268	16.4352003	0.4865	-18.65 ± 0.04	1.77 ± 0.40^H	76 ± 3	11.7 ± 2.7	0.73 ± 1.6	...	...
WLTV J001830.64+162642.9	4.6276554	16.4452699	0.6533	-19.83 ± 0.05	2.35 ± 0.80^H	23 ± 3	1.5 ± 0.6	2.00 ± 1.2	...	...
WLTV J001834.30+162648.9	4.6429167	16.4469257	0.6926	-19.76 ± 0.04	2.56 ± 0.62^H	78 ± 7	17.5 ± 4.6	1.48 ± 0.3	18.32 ± 0.3	8.2 ± 0.2
WLTV J001835.19+162658.8	4.6466418	16.4496750	0.4858	-18.95 ± 0.05	1.85 ± 0.40^H	< 10	0.2 ± 0.1	0.35 ± 0.5	...	8.6 ± 1.8
WLTV J001835.82+162611.4	4.6492322	16.4365057	0.6227	-19.95 ± 0.06	1.37 ± 0.69^W	109 ± 13	18.2 ± 9.4	4.92 ± 2.1	...	...
WLTV J001844.66+162459.9	4.6860672	16.4166487	0.8330	-20.58 ± 0.04	4.33 ± 1.23^H	102 ± 55	50.5 ± 31.2	3.24 ± 0.5	10.48 ± 0.5	7.4 ± 0.4
WLTV J001846.64+162547.3	4.6943428	16.4298197	0.4384	-20.36 ± 0.04	1.54 ± 0.01^H	42 ± 1	3.1 ± 0.1	2.32 ± 0.1	4.49 ± 0.8	8.8 ± 0.0
WLTV J001819.48+162533.1	4.5811615	16.4258787	0.8269	-20.84 ± 0.05	9.11 ± 3.49^H	54 ± 12	30.0 ± 13.3	8.58 ± 5.3	...	5.8 ± 0.7
WLTV J045354.78-030203.9	73.4782672	-3.0344341	0.7190	-20.12 ± 0.04	1.94 ± 0.05^H	126 ± 7	34.9 ± 2.2	3.37 ± 0.6	...	...
WLTV J045358.38-025618.5	73.4932513	-2.9384845	0.8255	-20.06 ± 0.04	2.96 ± 0.64^H	66 ± 68	14.4 ± 15.3	2.69 ± 0.4	...	6.9 ± 0.4
WLTV J045359.94-030306.1	73.4997697	-3.0516944	0.5679	-19.65 ± 0.05	2.62 ± 0.33^H	96 ± 12	27.1 ± 4.8	0.67 ± 0.3	12.55 ± 0.5	...
WLTV J045400.93-030312.6	73.5038636	-3.0535020	0.5697	-21.43 ± 0.04	2.96 ± 0.14^H	54 ± 3	9.7 ± 0.8	3.12 ± 2.2	27.45 ± 0.2	...
WLTV J045402.65-025918.4	73.5110531	-2.9884637	0.7150	-19.61 ± 0.04	1.21 ± 0.23^H	43 ± 4	2.5 ± 0.5	1.04 ± 0.2	...	7.8 ± 0.4
WLTV J045405.49-030202.4	73.5228918	-3.0340243	0.5689	-18.90 ± 0.05	1.04 ± 0.20^H	48 ± 4	2.8 ± 0.6	0.38 ± 0.1	...	...
WLTV J045407.09-025837.4	73.5295585	-2.9770594	0.5674	-20.03 ± 0.04	1.23 ± 0.12^H	29 ± 5	1.2 ± 0.2	1.03 ± 0.7	...	...
WLTV J045407.76-030055.5	73.5323133	-3.0154195	0.5677	-20.93 ± 0.04	4.34 ± 0.47^H	118 ± 4	67.6 ± 7.7	2.79 ± 0.1	...	...
WLTV J045409.67-030232.2	73.5403107	-3.0423026	0.3545	-19.98 ± 0.04	2.12 ± 0.07^H	15 ± 2	0.5 ± 0.1	1.62 ± 0.1	6.36 ± 0.6	8.3 ± 0.1
WLTV J045409.67-030043.0	73.5402878	-3.0119636	0.4439	-18.65 ± 0.04	2.48 ± 1.33^H	29 ± 3	2.5 ± 1.3	0.31 ± 0.1	3.71 ± 0.8	7.4 ± 1.3
WLTV J045411.02-030125.6	73.5459121	-3.0238001	0.5896	-20.11 ± 0.04	1.20 ± 0.05^H	35 ± 1	1.7 ± 0.1	3.15 ± 0.4	10.90 ± 0.4	8.8 ± 0.2
WLTV J045410.97-025913.8	73.5457235	-2.9871760	0.9865	-21.36 ± 0.04	0.31 ± 0.02^H	62 ± 10	1.4 ± 0.3	15.77 ± 1.7	...	5.4 ± 0.4
WLTV J045412.21-030328.2	73.5508668	-3.0578372	0.6548	-20.63 ± 0.04	1.40 ± 0.70^W	87 ± 10	11.9 ± 6.2	1.83 ± 0.2	16.54 ± 0.3	9.0 ± 0.4
WLTV J045412.10-030325.0	73.5504014	-3.0572215	0.6554	-20.43 ± 0.04	3.52 ± 0.52^H	89 ± 30	31.2 ± 11.7	1.58 ± 0.2	19.75 ± 0.3	8.9 ± 0.3
WLTV J045415.68-030411.9	73.5653136	-3.0699730	0.7760	-20.45 ± 0.04	2.66 ± 0.30^H	36 ± 5	4.0 ± 0.7	1.82 ± 0.2	6.66 ± 0.6	8.1 ± 0.4
WLTV J045420.19-030346.8	73.5841290	-3.0630249	0.6186	-20.52 ± 0.04	1.93 ± 0.13^H	69 ± 3	10.4 ± 0.8	3.15 ± 0.3	...	8.6 ± 0.5
WLTV J045420.57-030517.2	73.5856996	-3.0881327	0.8183	-20.77 ± 0.04	2.77 ± 0.24^H	56 ± 5	9.7 ± 1.2	1.69 ± 0.3	13.63 ± 0.4	8.4 ± 0.4
WLTV J045422.66-030503.1	73.5944373	-3.0842073	0.5799	-20.23 ± 0.04	2.62 ± 0.22^H	80 ± 5	19.0 ± 2.0	1.83 ± 0.3	...	8.9 ± 0.2
WLTV J045422.73-030416.3	73.5947091	-3.0712078	0.8848	-20.37 ± 0.05	2.17 ± 0.32^H	146 ± 7	52.0 ± 8.1	2.57 ± 0.4	14.93 ± 0.6	7.5 ± 0.4
WLTV J045424.70-030303.6	73.6029358	-3.0510237	0.9860	-20.49 ± 0.04	4.34 ± 0.81^W	62 ± 42	19.1 ± 13.4	5.57 ± 1.2	...	6.1 ± 0.4
WLTV J045425.76-030513.9	73.6073246	-3.0871954	0.7330	-20.76 ± 0.04	3.44 ± 0.05^H	69 ± 7	18.8 ± 2.1	4.76 ± 0.4	...	7.0 ± 0.3
WLTV J045427.31-025831.5	73.6137908	-2.9754424	0.5778	-18.71 ± 0.05	2.00 ± 0.48^H	38 ± 5	3.3 ± 0.9	0.76 ± 0.4	...	8.7 ± 2.0
WLTV J132435.56+301124.8	201.1481469	30.1902250	0.7815	-20.19 ± 0.04	1.50 ± 0.75^W	73 ± 6	9.1 ± 4.6	2.18 ± 0.1	...	7.5 ± 0.3
WLTV J132446.14+301020.9	201.1922365	30.1724843	0.7015	-20.15 ± 0.04	3.16 ± 0.72^W	79 ± 13	22.2 ± 6.3	1.07 ± 0.2	...	...
WLTV J132456.78+301159.2	201.2365773	30.1997992	0.5940	-18.77 ± 0.05	2.38 ± 0.67^W	74 ± 9	14.9 ± 4.6	0.01 ± 0.0	...	9.0 ± 1.8
WLTV J132457.29+301157.8	201.2387127	30.1994066	0.7998	-19.71 ± 0.04	3.12 ± 0.76^W	46 ± 5	7.4 ± 2.0	1.56 ± 0.5	...	7.3 ± 0.5
WLTV J132458.04+301115.5	201.2418274	30.1876456	0.7849	-19.54 ± 0.04	3.49 ± 0.76^W	41 ± 10	6.8 ± 2.3	1.30 ± 0.2	...	8.9 ± 0.7
WLTV J132458.78+301136.3	201.2449283	30.1934218	0.7998	-19.50 ± 0.04	3.22 ± 0.76^W	45 ± 5	7.4 ± 1.9	1.06 ± 0.2	...	6.6 ± 1.4
WLTV J132500.25+300853.2	201.2510585	30.1481219	0.6180	-20.85 ± 0.04	3.68 ± 0.69^W	75 ± 2	23.7 ± 4.5	0.09 ± 0.1	...	9.1 ± 1.0
WLTV J132505.84+301200.6	201.2743179	30.2001930	0.8383	-20.12 ± 0.05	3.17 ± 0.77^W	66 ± 11	15.7 ± 4.6	1.52 ± 0.2	...	7.9 ± 0.4
WLTV J132509.33+301010.6	201.2888767	30.1696218	0.6070	-21.06 ± 0.04	3.73 ± 0.68^W	50 ± 3	10.5 ± 2.0	0.10 ± 0.1	...	9.2 ± 1.0
WLTV J132515.80+301111.8	201.3158279	30.1866204	0.8402	-21.26 ± 30.00	1.54 ± 0.94^W	59 ± 6	6.1 ± 3.8	5.29 ± 0.3	...	7.7 ± 0.3
WLTV J132520.16+301107.7	201.3340026	30.1854901	0.6591	-20.92 ± 0.04	3.35 ± 0.71^W	75 ± 1	21.1 ± 4.5	7.66 ± 0.1	...	8.7 ± 0.0
WLTV J132524.05+301021.6	201.3502129	30.1726779	0.6597	-19.75 ± 0.04	2.89 ± 0.71^W	93 ± 6	27.9 ± 7.1	0.03 ± 0.0	...	9.0 ± 1.0

Table 2—Continued

Object (1)	α (J2000) (2)	β (J2000) (3)	z (4)	M_B (mag) (5)	r_e (kpc) (6)	σ ($km\ s^{-1}$) (7)	Mass ($10^9\ M_\odot$) (8)	SFR(OII) ($M_\odot\ yr^{-1}$) (9)	SFR(IR) ($M_\odot\ yr^{-1}$) (10)	12+log(O/H) (dex) (11)
WLTV J132524.70+301213.2	201.3529109	30.2036743	0.6075	-20.78 ± 0.04	3.14 ± 0.68^W	79 ± 3	22.3 ± 4.9	0.08 ± 0.1	...	9.0 ± 1.0
WLTV J132529.04+300734.6	201.3710158	30.1262793	0.9203	-18.79 ± 0.04	1.58 ± 0.80^W	63 ± 5	7.0 ± 3.6	0.60 ± 0.0	...	7.5 ± 0.3
WLTV J132538.84+301048.2	201.4118496	30.1800576	0.6979	-20.86 ± 0.04	3.52 ± 0.72^W	62 ± 3	15.6 ± 3.3	0.09 ± 0.1	...	9.3 ± 1.1
WLTV J160350.90+430654.6	240.9620764	43.1151916	0.8314	-19.46 ± 0.11	1.53 ± 0.78^W	43 ± 3	3.2 ± 1.6	0.02 ± 0.0	...	...
WLTV J160351.75+430748.7	240.9656222	43.1302128	0.8610	-20.14 ± 0.05	4.50 ± 0.78^W	54 ± 5	14.9 ± 3.0	2.50 ± 0.5	...	8.6 ± 1.9
WLTV J160408.43+430009.8	241.0351107	43.0027345	0.5798	-19.87 ± 0.04	3.54 ± 0.66^W	43 ± 3	7.6 ± 1.6	0.03 ± 0.0	1.59 ± 0.5	9.3 ± 1.1
WLTV J160415.93+430618.1	241.0663830	43.1050541	0.8290	-19.16 ± 0.06	2.66 ± 0.77^W	34 ± 3	3.6 ± 1.1	0.02 ± 0.0	...	...
WLTV J160422.15+430542.5	241.0922999	43.0951607	0.8300	-21.05 ± 0.04	4.48 ± 1.57^H	72 ± 5	26.2 ± 9.4	4.63 ± 0.4	...	...
WLTV J160427.90+430401.9	241.1162686	43.0672186	0.8275	-19.28 ± 0.09	1.99 ± 1.10^H	124 ± 20	34.1 ± 19.8	0.86 ± 0.9	15.89 ± 0.1	...
WLTV J160428.02+430007.4	241.1167467	43.0020768	0.7441	-22.08 ± 0.06	1.87 ± 0.74^W	57 ± 4	6.8 ± 2.8	0.26 ± 0.3	...	...
WLTV J160429.08+425955.0	241.1211631	42.9986169	0.7507	-18.97 ± 0.06	3.03 ± 0.74^W	52 ± 6	9.3 ± 2.6	0.02 ± 0.0	6.23 ± 0.2	9.1 ± 1.9
WLTV J160433.16+430452.7	241.1381739	43.0813248	0.8665	-18.80 ± 0.08	2.81 ± 0.29^H	34 ± 6	3.7 ± 0.8	0.58 ± 0.6	...	...
WLTV J160442.65+430827.8	241.1777033	43.1410584	0.6203	-19.68 ± 0.05	2.71 ± 0.68^W	40 ± 4	4.9 ± 1.3	0.03 ± 0.0	12.80 ± 0.2	...
WLTV J160429.42+425945.7	241.1225975	42.9960265	0.5882	-20.47 ± 0.04	2.88 ± 0.67^W	45 ± 2	6.6 ± 1.6	0.06 ± 0.1	...	9.0 ± 1.0
WLTV J160446.27+431023.5	241.1927985	43.1732114	0.6948	-19.34 ± 0.74	1.92 ± 0.72^W	32 ± 1	2.2 ± 0.8	0.02 ± 0.0	...	8.6 ± 1.5
Cluster Blue Galaxy										
WLTV J001813.32+162440.8	4.5555066	16.4113337	0.5450	-21.29 ± 0.04	9.34 ± 0.65^W	...	...	1.61 ± 0.1	...	8.7 ± 0.1
WLTV J001813.61+162455.0	4.5567216	16.4153018	0.5454	-20.89 ± 0.04	4.72 ± 0.64^W	...	...	1.42 ± 0.1	...	9.0 ± 0.1
WLTV J001814.69+162426.2	4.5612138	16.4073028	0.5491	-21.43 ± 0.04	8.07 ± 0.65^W	...	...	1.39 ± 0.1	...	9.0 ± 0.1
WLTV J001816.48+162547.2	4.5686686	16.4297923	0.5467	-19.17 ± 0.06	7.15 ± 0.65^W	...	...	1.76 ± 1.5	...	8.6 ± 1.0
WLTV J001819.21+162415.6	4.5800526	16.4043495	0.5463	-19.47 ± 0.04	4.03 ± 0.89^H	...	...	0.85 ± 0.3	...	8.6 ± 0.9
WLTV J001820.09+162318.9	4.5836895	16.3885837	0.5728	-20.64 ± 0.04	2.58 ± 0.14^H	...	...	1.15 ± 0.2	...	...
WLTV J001822.44+162531.6	4.5934932	16.4254592	0.5442	-20.51 ± 0.04	17.20 ± 0.67^W	...	...	1.15 ± 0.5	...	...
WLTV J001823.68+162502.6	4.5986727	16.4174012	0.5516	-18.83 ± 0.06	1.47 ± 0.59^H	...	...	0.67 ± 0.5	...	9.0 ± 1.4
WLTV J001824.22+162513.2	4.6008981	16.4203332	0.5526	-19.49 ± 0.04	1.68 ± 0.26^H	...	...	1.10 ± 0.1	...	8.9 ± 0.1
WLTV J001836.54+162515.1	4.6522550	16.4208647	0.5532	-20.02 ± 0.04	3.46 ± 0.67^H	...	...	0.10 ± 0.0	...	...
WLTV J001840.20+162506.6	4.6674911	16.4185034	0.5381	-20.19 ± 0.04	3.09 ± 0.03^H	...	...	1.40 ± 0.2	...	7.9 ± 0.2
WLTV J001845.29+162706.5	4.6886946	16.4518150	0.5385	-21.08 ± 0.04	7.16 ± 0.64^W	...	...	7.48 ± 0.7	...	8.6 ± 0.2
WLTV J001848.15+162556.1	4.7006305	16.4322493	0.5325	-19.57 ± 0.05	5.34 ± 0.64^W	...	...	0.59 ± 0.2	...	...
WLTV J045358.36-030126.6	73.4931775	-3.0240815	0.5369	-19.82 ± 0.05	4.43 ± 0.10^H	...	...	0.88 ± 0.1	...	8.4 ± 0.2
WLTV J045358.88-025828.0	73.4953229	-2.9744572	0.5081	-18.38 ± 0.05	2.15 ± 0.62^W	...	...	0.18 ± 0.2	...	8.6 ± 1.9
WLTV J045359.56-025803.5	73.4981627	-2.9676489	0.5511	-20.84 ± 0.04	5.65 ± 0.55^H	...	...	1.16 ± 0.1	...	...
WLTV J045400.13-030207.8	73.5005414	-3.0355113	0.5482	-18.44 ± 0.05	1.63 ± 0.39^H	...	...	0.65 ± 0.2	...	8.4 ± 0.7
WLTV J045401.41-025859.8	73.5058703	-2.9833001	0.5314	-19.58 ± 0.04	2.96 ± 1.42^H	...	...	0.68 ± 0.1	...	8.7 ± 0.3
WLTV J045404.50-030013.6	73.5187366	-3.0037808	0.5322	-21.41 ± 0.04	7.39 ± 0.38^H	...	...	2.31 ± 0.1	...	8.8 ± 0.0
WLTV J045406.77-030031.4	73.5282151	-3.0087413	0.5453	-20.35 ± 0.04	3.84 ± 0.91^H	...	...	1.32 ± 0.2	...	8.9 ± 0.2
WLTV J045415.86-030356.1	73.5660694	-3.0656041	0.5260	-20.78 ± 0.04	5.05 ± 0.48^H	...	...	3.12 ± 0.1	...	8.9 ± 0.1
WLTV J045428.96-030506.8	73.6206506	-3.0852374	0.5086	-19.60 ± 0.04	4.24 ± 1.06^H	...	...	0.73 ± 0.1	...	7.7 ± 0.7
WLTV J105638.95-034041.1	164.1623084	-3.6781093	0.8298	-19.51 ± 0.08	6.07 ± 0.77^W	...	...	1.16 ± 0.8	...	...
WLTV J105644.75-033348.8	164.1864420	-3.5635784	0.8340	-19.19 ± 0.09	5.85 ± 2.54^H	...	...	0.68 ± 0.2	...	...
WLTV J105702.54-033948.1	164.2605863	-3.6633828	0.8320	-20.28 ± 0.07	5.26 ± 0.77^W	...	...	1.88 ± 1.9	...	...
WLTV J105704.45-033515.9	164.2685356	-3.5877566	0.8268	-19.35 ± 0.06	2.76 ± 0.89^H	...	...	1.35 ± 0.5	...	...
WLTV J105707.27-033538.6	164.2802861	-3.5940554	0.8410	-20.16 ± 0.04	1.79 ± 0.59^H	...	...	1.51 ± 0.4	...	...
WLTV J105708.46-033512.3	164.2852546	-3.5867494	0.8374	-20.12 ± 0.06	4.46 ± 1.05^H	...	...	0.94 ± 0.4	...	...
WLTV J105711.46-033540.5	164.2977662	-3.5945981	0.8392	-16.52 ± 0.07	2.54 ± 0.06^H	...	...	0.04 ± 0.0	...	...
WLTV J105713.91-033548.1	164.3079645	-3.5967120	0.8307	-20.20 ± 0.09	2.00 ± 0.77^W	...	...	1.69 ± 0.5	...	...
WLTV J132436.19+300843.1	201.1507784	30.1453114	0.7528	-20.48 ± 0.04	5.72 ± 0.74^W	...	...	4.58 ± 0.3	...	8.7 ± 0.3
WLTV J132440.55+301043.1	201.1689704	30.1786405	0.7552	-20.25 ± 0.05	6.62 ± 0.75^W	...	...	1.27 ± 0.1	...	...

Table 2—Continued

Object	α (J2000)	β (J2000)	z	M_B (mag)	r_e (kpc)	σ ($km\ s^{-1}$)	Mass ($10^9\ M_\odot$)	SFR(OII) ($M_\odot\ yr^{-1}$)	SFR(IR) ($M_\odot\ yr^{-1}$)	12+log(O/H) (dex)
(1)	(2)	(3)	(4)	(5)	(6)	(7)	(8)	(9)	(10)	(11)
WLTV J132440.31+301114.7	201.1679695	30.1874284	0.7580	-18.99 ± 0.06	3.16 ± 0.75^W	...	...	0.64 ± 0.2	...	...
WLTV J132442.46+300922.8	201.1769086	30.1563440	0.7562	-18.84 ± 0.08	3.73 ± 0.75^W	...	...	0.64 ± 0.1	...	...
WLTV J132448.20+301103.2	201.2008414	30.1842277	0.7621	-20.94 ± 0.04	7.60 ± 0.75^W	...	...	1.10 ± 0.1	...	7.5 ± 0.6
WLTV J132449.26+301115.6	201.2052417	30.1876712	0.7493	-21.14 ± 0.04	1.48 ± 0.74^W	...	...	2.63 ± 0.2	...	8.8 ± 0.5
WLTV J132450.90+300822.4	201.2120723	30.1395759	0.7575	-18.30 ± 0.08	2.53 ± 0.75^W	...	...	0.37 ± 0.6	...	...
WLTV J132501.60+301147.2	201.2566720	30.1964475	0.7538	-20.60 ± 0.04	5.05 ± 0.74^W	...	...	3.35 ± 0.2	...	8.7 ± 0.3
WLTV J132504.26+301140.8	201.2677703	30.1946767	0.7557	-20.09 ± 0.05	7.89 ± 0.75^W	...	...	1.01 ± 0.2	...	8.7 ± 1.3
WLTV J132513.12+300906.3	201.3046708	30.1517526	0.7369	-20.91 ± 0.06	7.03 ± 0.74^W	...	...	4.16 ± 0.1	...	8.4 ± 0.2
WLTV J132537.93+300844.1	201.4080236	30.1455895	0.7210	-19.22 ± 0.05	1.46 ± 0.73^W	...	...	0.02 ± 0.0	...	...
WLTV J160354.27+430744.8	240.9761376	43.1291212	0.8742	-18.68 ± 0.06	4.18 ± 0.78^W	...	...	0.68 ± 0.3	...	...
WLTV J160409.68+430248.6	241.0403379	43.0468537	0.9102	-21.82 ± 0.06	9.56 ± 0.79^W	...	...	3.49 ± 1.1	...	...
WLTV J160409.73+430711.9	241.0405555	43.1199890	0.8985	-21.39 ± 0.08	16.30 ± 0.80^W	...	...	13.56 ± 11.0	...	...
WLTV J160410.03+430358.4	241.0417980	43.0662410	0.9089	-20.50 ± 0.05	16.91 ± 0.80^W	...	...	3.94 ± 4.6	...	...
WLTV J160410.69+430430.3	241.0445465	43.0750950	0.9069	-19.47 ± 0.05	5.26 ± 0.79^W	...	...	1.96 ± 0.4	...	...
WLTV J160417.27+430654.0	241.0719602	43.1150006	0.9085	-16.33 ± 0.06	7.27 ± 0.79^W	...	...	0.10 ± 0.1	...	...
WLTV J160431.37+430616.8	241.1307060	43.1046845	0.8960	-18.93 ± 0.09	3.86 ± 0.79^W	...	...	0.49 ± 0.2	...	9.1 ± 1.2
WLTV J160431.98+430554.4	241.1332349	43.0984543	0.9173	-19.77 ± 0.07	3.24 ± 0.80^W	...	...	2.18 ± 0.4	...	6.7 ± 0.4
WLTV J160432.07+430713.3	241.1336345	43.1203664	0.9002	-21.35 ± 0.06	6.92 ± 0.79^W	...	...	6.36 ± 8.9	...	...
WLTV J160433.57+430813.8	241.1398813	43.1371722	0.8982	-18.59 ± 0.09	4.30 ± 0.79^W	...	...	0.59 ± 0.1	...	...

Note. — (1) Identification in WLTV survey (2) Right Ascension (3) Declination (4) redshift (5) Absolute B-band magnitude (6) Half-light radius (7) Velocity dispersion (8) Dynamical Mass (9) SFR from OIIλ3727 (10) SFR from 24 μmm flux (11) Oxygen Abundance

3.1. Photometry

We measured aperture and total magnitudes for each source from the ground-based and HST imaging data following the procedure described in Crawford et al. (2009). For the aperture photometry measurements using the ground-based data only, we convolved the ground-based images with a 2-D Gaussian function to match the seeing of the worst band for that cluster so that the apertures would be sampling the same light profiles in the different bands. To define aperture magnitudes, we set the photometric aperture to a diameter of 7.5 kpc at the redshift of the cluster, the size corresponding to the average disk scale length of an L^* galaxy.

For the total magnitudes, we use the same methodology as in our previous work (Crawford et al. 2006, 2009). We measured the total magnitude within an aperture that would enclose 99% of the light based on the profile shape of the source. The profile shape of the source is determined by measuring the concentration index, C_{2080}. Following Kent (1984) and Bershady et al. (2000), we define C_{2080} as

$$C_{2080} = 5\log(r_{20}/r_{80}) \tag{1}$$

where r_n is the radius that encloses n% of the light.

3.2. Size

We derived the half-light radius (r_{50}) for each source from the curve of growth we constructed in measuring the total magnitudes. We measured the radius in both the ground-based and HST images.

Although the HST images offer superior spatial resolution, they do not cover a wide projected area and hence miss many objects in our survey. In contrast, the lower-resolution WIYN images permit us to measure sizes for more objects. We used the sizes measured independently from WIYN and HST to establish the accuracy of the sizes derived from the ground-based images. A simple quadrature subtraction of the seeing value as measured from stellar objects in the WIYN frames returns a reasonable measurement of the size, as depicted in Figure 1. The median difference between the WIYN measurements and the HST measurements is $0\farcs065$, although significant scatter exists at values less than $0\farcs3$.

Whenever possible, we used the half-light radius as measured in the HST data. We have not rejected any objects based on the source of their size measurements. The provenance of the size measurement is indicated in the table.

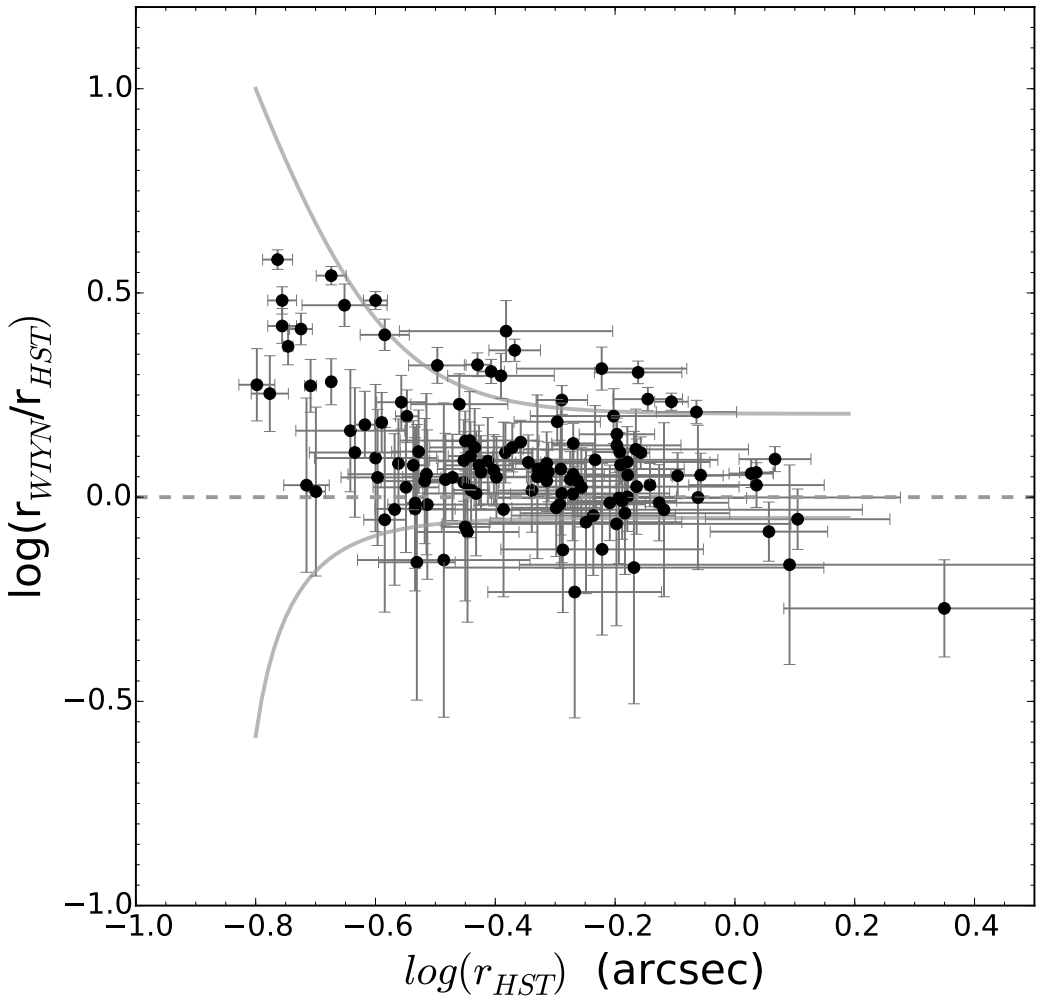

Fig. 1.— Comparison between corrected half-light measurements from WIYN observations and HST observations for LCBGs as a function of HST half-light radius. The corrected WIYN r_e values are consistent with the HST measurements with a median difference of $0\farcs07$. This is consistent with a proportional offset of 20% and a rms scatter of 25% within the critical half-light size range of 0.3 to 3 arcsec. Solid lines approximate this offset and scatter. The precision and accuracy is more than adequate for our characterization of LCBG size and surface-brightness.

3.3. Rest-Frame Properties

For each of our sources, we determined the absolute B-band magnitude, the rest-frame colors of the sources, and the size. To determine the rest-frame magnitude and colors, we fit the spectral energy distribution (SED) of each galaxy to a range of artificial templates generated from GALEV (Bruzual & Charlot 2003) and empirical galaxy templates. To calculate M_B, we derive the K-correction for that model between the rest-frame B band and the passband closest to the redshift B band. For example, for a galaxy at $z = 0.54$, the rest-frame B band is closest to the observed R band, and so the K-correction is calculated and applied to the apparent total R-band magnitude. A similar process is used for the rest-frame colors, but we use the aperture magnitudes instead of the total magnitudes. We applied the appropriate cosmological corrections in converting angular measures of size to absolute radii.

3.4. Velocity Width

The superb wavelength resolution (10 km s^{-1}) of the Keck DEIMOS spectra permit us to measure the velocity widths of even the narrowest of the galaxies in our sample based on their emission lines, greatly enhancing the utility of our study For each spectroscopic source, we fit either single or double Gaussian functions to the emission lines associated with [O II] λ3727, Hβ, and [O III] λ5007. We performed the fit after after subtracting off a low-order polynomial fit to the continuum of the spectrum near the feature of interest. The DEIMOS spectra resolved the [O II] λ3727 doublet into two components, allowing us to fit a double Gaussian with the line separation fixed in the rest frame but the remaining parameters allowed to vary. We visually inspected all fits to confirm quality.

To correct for instrumental effects, we follow the procedure from Guzmán et al. (1997) and subtract, in quadrature, the instrumental dispersion from the measured value to recover the intrinsic velocity dispersion of the galaxy. For most sources, we estimated the instrumental dispersion based on measurements of nearby sky lines. For one mask (`w05.m2`), the seeing during the observations was exceptional and compact sources did not fill the slit uniformly. For compact targets on this mask, the velocity dispersion for all lines was well below the value measured for the sky lines in the spectra. For these sources, we estimated their image size based on their spatial extent in the slit and corrected the dispersion of the sky lines assuming the effective slit size was equivalent to the full-width half maximum of the image size. Similar undersampling problems could affect additional masks in our survey, so for our most compact sources we may be underestimating the velocity dispersion. In addition, we did not correct the fits for absorption or for any observed rotation or irregularities in the line

profiles. In the worst case, this would introduce an uncertainty of approximately a factor of ~ 2. Out of all our spectroscopic sources, only $\sim 25\%$ showed visual evidence of rotation.

After correcting for the instrumental effects, we determined the final velocity width of each source by calculating the weighted average of the measurements for the three lines. The weights are based on the inverse variance for each of the lines. The average velocity dispersion from all of the lines is reported in Table 3. Errors for each source were based on combining errors from each line in quadrature. We estimate that the smallest velocity dispersion that we can safely recover is 10 km s^{-1} based on the instrumental velocity dispersion. Any value below this is reported as an upper limit.

3.5. Galaxy Mass

Using the average velocity width and best size measurement, we calculated the dynamical mass of each system following Phillips et al. (1997) as:

$$M_{dyn} = \frac{3c_2}{G}\sigma_v^2 r_e, \tag{2}$$

where we take c2, a geometric factor, to be 1.6. This equation is based on an assumption of a virialized system, but, to within a factor of 1.4, it should give a similar result as for a rotational supported system (Phillips et al. 1997) .

In addition, we correct the velocity dispersion for a factor of 1.3 following Guzmán et al. (2003) to correct for the difference between measuring emission lines instead of stellar absorption lines. When our data lack sufficient resolution to determine the velocity width and size of certain sources, we report only upper limits on dynamical mass in Table 3.

3.6. Equivalent Width

We followed two methods to measure the equivalent width (EW). The first method calculates the continuum level within two regions lying outside of the line of interest, and then computes the sum over a region that includes the line of interest to estimate the line flux. The summed region was designed to include all of the line flux while avoiding any of the line flux in the continuum measurements. The second method is based on integrating the Gaussian function fit to all of our emission lines while measuring the velocity width (see the previous sections for details of the velocity width measurement). The lines that we measured include [O II] λ3727, Hβ, and [O III] λ5007. Both techniques yield comparable results with a standard deviation of 15%. We adopt the first method for our EW values presented here.

3.7. Star-Formation Rate

For comparison with Guzmán et al. (1997), we follow the process outlined in their appendix for converting [O II] λ3727 EW to star-formation rate (SFR). We apply the following formula to our data to estimate the SFR:

$$\mathrm{SFR}(M_\odot\ \mathrm{yr}^{-1}) = 2.5 \times 10^{-0.4(M_B - M_{B\odot})} \mathrm{EW}_{3727} \quad (3)$$

where M_B is the absolute B-band magnitude and EW_{3727} is the [O II] λ3727 EW. This equation also includes a factor for the average extinction in blue galaxies. The SFR is a factor of ~ 3 lower compared to the Hα calibration from Kennicutt (1992) due to the more "top-heavy" IMF in Alonso-Herrero et al. (1996) with an upper mass limit of $M < 125\ M_\odot$ compared to $M < 100\ M_\odot$ in the previous work. Values for the SFR are listed in Table 3.

In addition to the SFR calculated from [O II] λ3727, we also calculate the $\mathrm{SFR}_{\mathrm{FIR}}$ based on the flux from the Spitzer 24 μm flux. We follow the method outlined in Rieke et al. (2009) and as applied in Randriamampandry et al. (2015) for converting the 24 μm flux to SFR based on their Equation 14 and Table 1.

3.8. Metallicity Measurements

We adopt the method of Kobulnicky & Kewley (2004) for measuring the metallicity of our objects. This variation on the R_{23} method (Pagel et al. 1979) uses the ratio of equivalent widths as opposed to flux ratios. Similar to other works, we corrected our Hβ EW by adding a value of 2 Å to it to account for stellar absorption and our total [O III] contribution was given by $1.3 \times \mathrm{EW}_{5007}$. From the values for R_{23} and O_{23}, we then used their Eq. 18 to calculate the $12 + \log[\mathrm{O/H}]$ metallicities for our galaxies. Unfortunately, degeneracies between the lines available for measuring the metallicity prevent us from distinguishing between the higher and lower metallicity tracks, but as in previous studies or star-forming sources (Kobulnicky & Kewley 2004) , we assume that LCBGs lie on the upper track with metallicities above $12 + \log[\mathrm{O/H}] = 8.4$. Regardless, we make the same assumptions for cluster and field sources so that comparison between the two are consistent.

4. Properties of LCBGs

4.1. Magnitude-Size Relationship

In Figure 2, we plot the relationship between magnitude and size for LCBGs and Blue Cloud (BC) galaxies. For comparison, we also plot the relationships found by Bamford et al. (2007) for low-redshift disk galaxies (dashed grey line) and intermediate redshift disk galaxies (solid grey line) in clusters. The first and most noticeable feature in the plot is that the LCBG galaxies exhibit smaller sizes at a given luminosity than normal disk galaxies both in the field and in clusters as expected from the definition of LCBGs.

The relationship fit to the low-redshift cluster sample by Bamford et al. (2007) was $\log_{10}(r_{50}) = -0.184 \times M_B - 3.081$. Likewise, we fit this same relationship to our data and, as they did, we fixed the slope of the relationship at a value of -0.184. We find that fitting a line of this slope to all cluster galaxies in our sample yields a best-fit intercept of 3.18 ± 0.03, which agrees (within the uncertainty) with what Bamford et al. found (3.20 ± 0.02) when they fit a similar line to their sample of intermediate-redshift cluster galaxies.

We note that if we exclude the LCBGs from our sample and re-fit the line, the derived intercept for the remaining Blue Cloud galaxies in our moderate-redshift *cluster* sample is comparable to the low-redshift *field* galaxy magnitude-size relationship from Bamford et al. (2007) with an intercept value of 3.11 ± 0.02. The shift to smaller sizes and more concentrated star formation found by Bamford et al. (2007) in intermediate clusters is possibly due not to changes in the star formation in individual disk galaxies, but rather to the increased presence of LCBGs in clusters (Crawford et al. 2011) that mimics the corresponding increase in number seen in the field (Guzmán et al. 1997).

The good agreement between the luminosity-size relationship for cluster and field LCBGs indicates the similarity in these two types of galaxies. As selected, LCBGs typically have smaller sizes at a given absolute magnitude than non-LCBG populations. Although there is a correlation between the size and luminosity, there is a considerable range in luminosity at any given size. Due to the extraordinary star formation occurring in some of the galaxies, some of those small-sized galaxies have magnitudes lying well above the relationship, thus producing asymmetric scatter about the line.

4.2. Comparison of Field and Cluster LCBGs

In Figure 3, we compare the size, absolute magnitude, mass, star-formation rates, and metallicity for cluster and field LCBGs. For the field sample, we used both the field sample

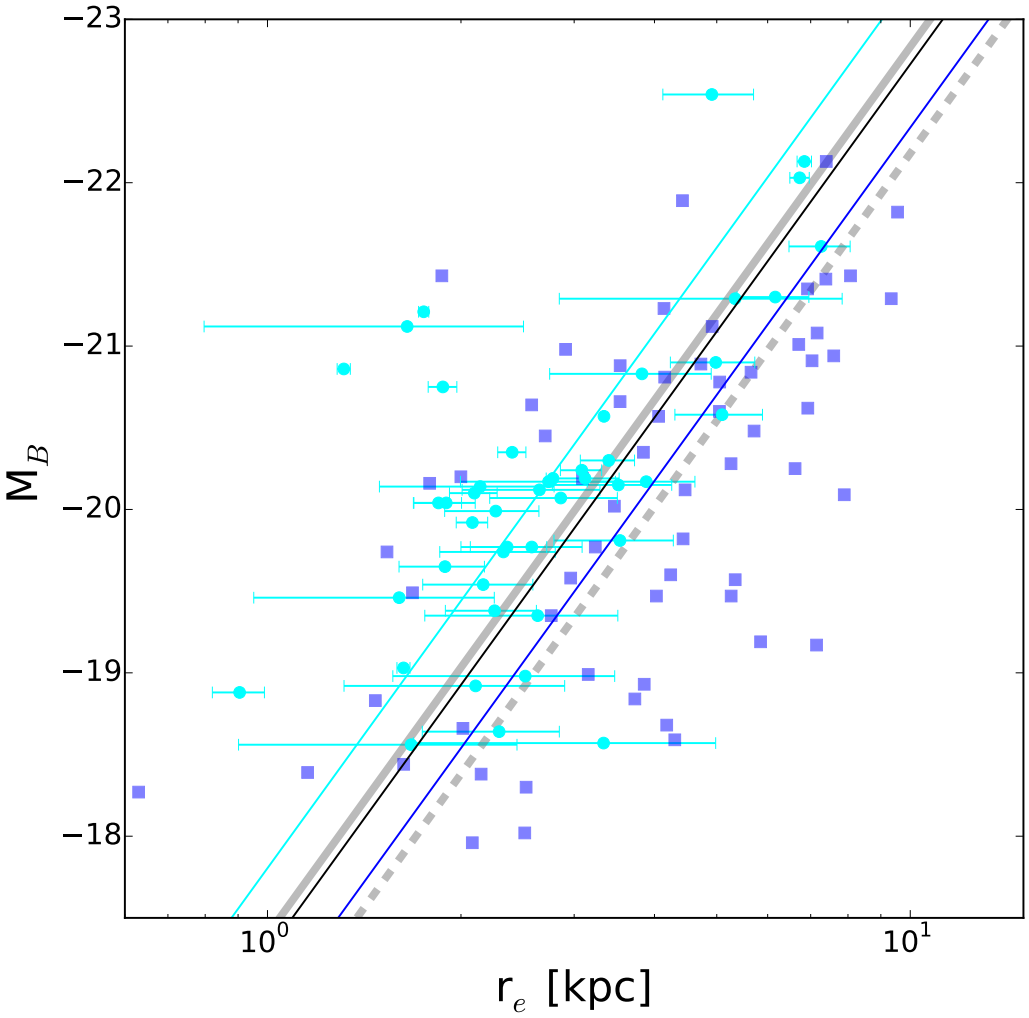

Fig. 2.— Magnitude-size relationship for cluster emission-line galaxies in our sample. Cluster LCBGs are represented as filled turquoise circles and cluster BC galaxies as filled blue squares. In addition, we plot the relationship for disk galaxies found by Bamford et al. (2007) in the low-redshift field (dashed, grey line) and in intermediate clusters (solid, grey line). Solid lines also represent the best-fit values for all of our sources (black line), LCBGs (turquoise line), and non-LCBG galaxies (blue line).

from our own observations and the sample from Guzmán et al. (1997), which has been selected in an identical manner as our cluster sample. We performed a Komolgorov-Smirnov test comparing the field and cluster samples; in all cases, the null hypothesis that the distributions were drawn from the same sample could not be rejected. We conclude that no difference between the key properties of LCBGs in our field and cluster samples is apparent.

4.3. Obscured Star formation in LCBGs

To explore the fraction of LCBGs with obscured star formation, we examined the SFR in our LCBGs from our sample with measured 24 μm fluxes in Figure 4. For the comparison, we have corrected our optical star-formation rate by a factor of 3 to account for differences in the assumptions about the IMF (see §3.7) . Although a number of sources exhibit equivalent SFR between the two methodologies, an equal number of sources show much higher star formation based on the FIR indicator. We attribute this discrepancy to the presence of obscuring dust in some LCBGs that preferentially absorbs optical radiation and causes the estimated SFR from optical and IR measurements to differ. We define "obscured" star-forming galaxies as those having $\mathrm{SFR_{FIR}} > 2 \times \mathrm{SFR_{3727}}$. Of the cluster sources measured, 44% show evidence for obscured star formation.

Applying an individual extinction correction to the [O II] λ3727-measured SFR may produce a stronger correlation between the two star-formation metrics. For example, Domínguez Sánchez et al. (2012) found good agreement between Hα SFR and $\mathrm{SFR_{FIR}}$ in galaxies with detections in both passbands only after correcting for the extinction at Hα in individual galaxies. Unfortunately, we lack the wavelength coverage or data quality to measure individual extinctions in each of our galaxies. However, we can make some statistical estimates.The galaxies with the bluest $(U-B)_o$ rest-frame colors, strongest $H\beta$ equivalent widths, and strongest [O III] λ5006 equivalent widths show no evidence of obscured star formation, whereas galaxies with weaker measurements show a range in the ratio of $\mathrm{SFR_{FIR}}$ to $\mathrm{SFR_{3727}}$.

We detect no significant difference in the fraction of galaxies exhibiting obscured star formation with $\sim 48\%$ of galaxies in both cluster and field environments showing obscured star formation. In addition, we measure no tendency for obscured star formation to be more or less common in objects at greater projected distances from the cluster center,, although the *Spitzer* images do not cover the full spatial extent of our clusters.

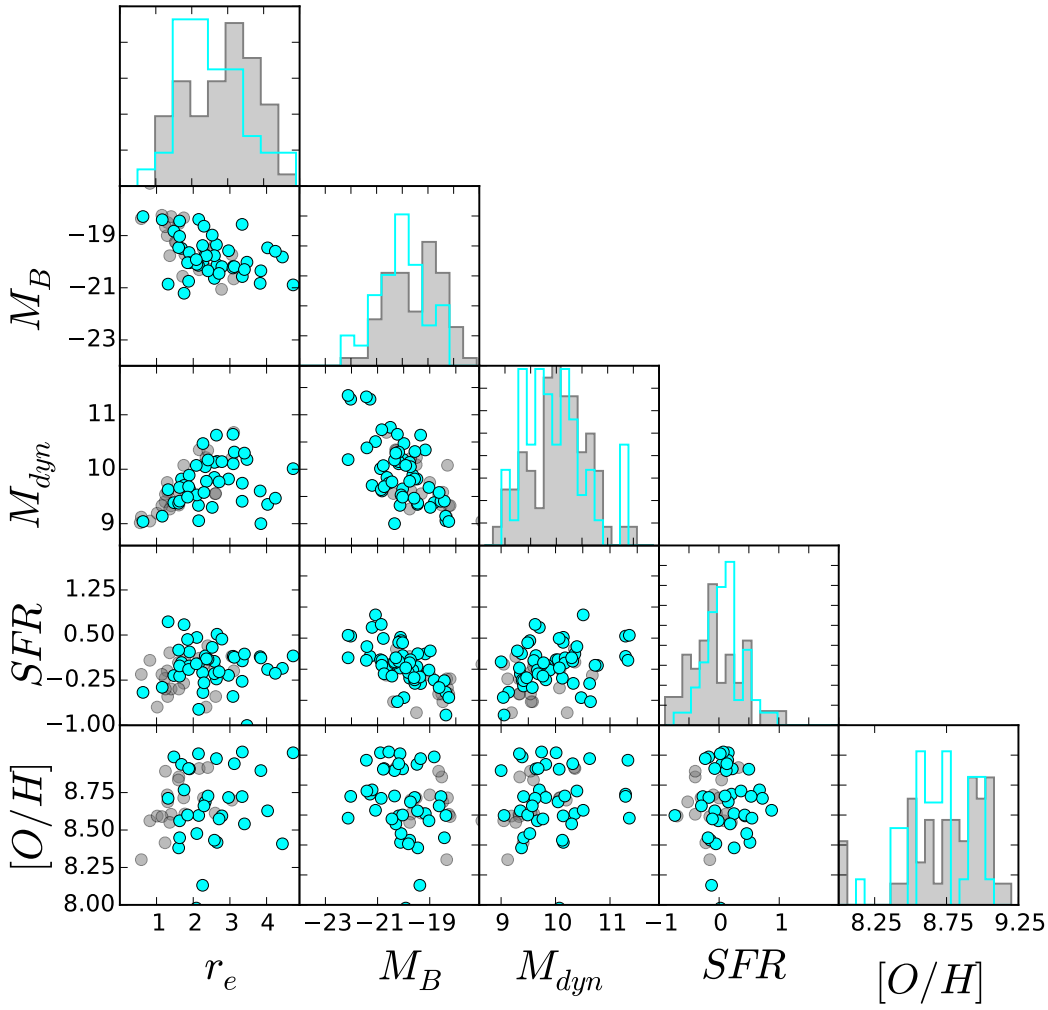

Fig. 3.— Comparison between the size, absolute magnitude, mass, and star formation rate for cluster and field LCBGs. LCBGs that are confirmed cluster members from our sample are plotted as turquoise circles. LCBGs from the field (both our sample and from Guzmán et al. (1997)) are plotted as grey circles. No significant difference between the field and cluster LCBG populations is evident.

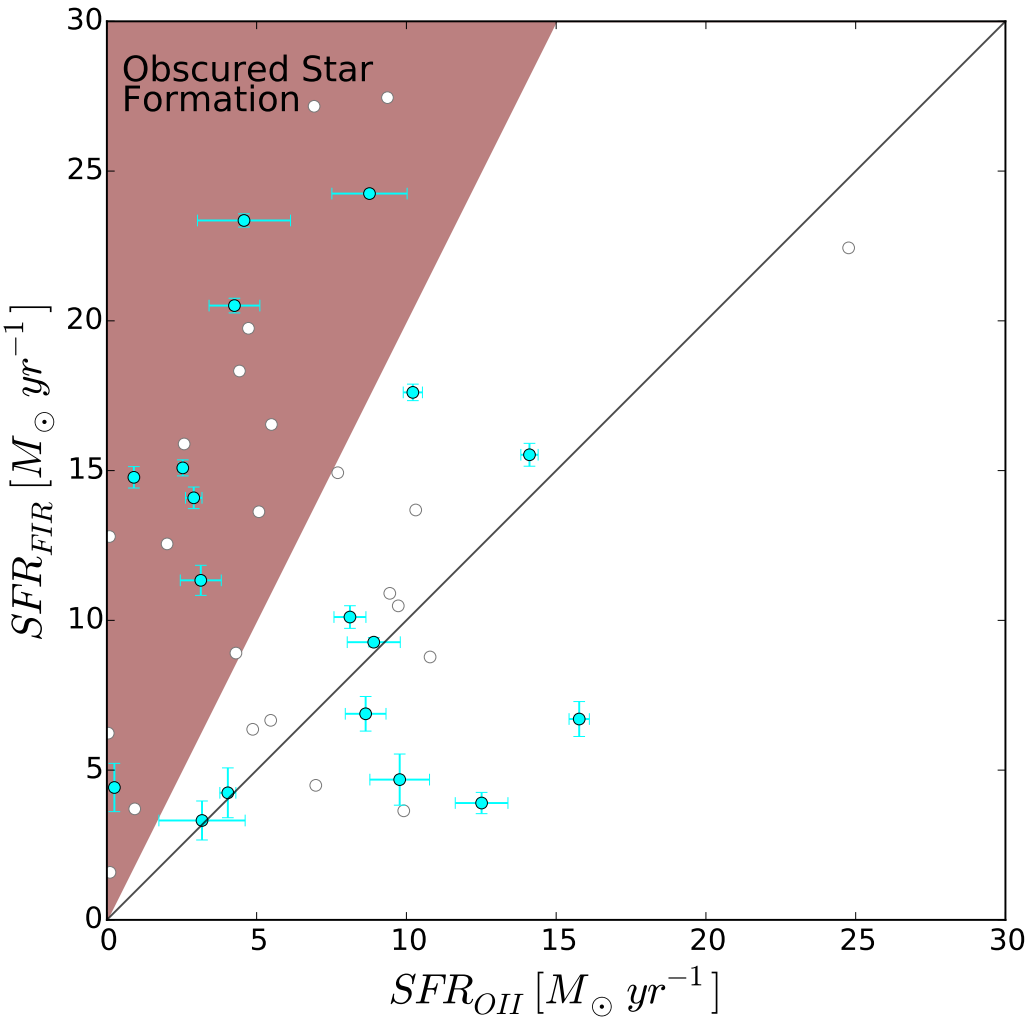

Fig. 4.— Comparison between star formation measured from [O II] λ3727 and 24 μm flux. Cluster (filled-teal circles) and field sources (empty-grey circles) are presented. Approximately 48% of both populations show evidence for obscured star formation. As indicated by the shaded region at top left, we define objects as showing evidence for obscured star formation if their 24 micron-derived SFR exceeds their optically-measured SFR by more than a factor of 2.

4.4. Trends with Cluster Radius

As we have previously shown (Crawford et al. 2006, 2014), LCBGs preferentially avoid the central regions of clusters. As can be seen in Figure 5, strongly-star-forming LCBGs seem to be largely absent within the cores of the clusters. The decrease in star-forming galaxies at small radii appears to begin around 0.5 R_{200}, and within 0.2 R_{200} there seems to be a complete lack of strong star-forming LCBGs. The distribution of SFR in our sample of intermediate-redshift LCBGs mimics the distribution seen for low-redshift star bursting galaxies by Mahajan et al. (2012) with a rise in star formation at larger radii followed by a decrease towards the cluster center.

Although the SFR as a function of radius for all types of galaxies shows a strong decrease towards the center of the cluster (Gómez et al. 2003), the SFR for galaxies that show evidence of star formation shows no trend with radius (Biviano et al. 1997; Finn et al. 2005; Bretherton et al. 2010). However, the overall SFR in cluster galaxies does tend to be less than that in the field at the same redshift (Balogh et al. 2002; Finn et al. 2005). For LCBGs, we see no difference in SFR between cluster and field for the population as a whole, but we do observe a steep decline with cluster radius. A similar trend is observed with the SFR_{IR} data as well but the limited field of view of the IR data makes it difficult to confirm the trend. If these sources are recent arrivals to the cluster, the star formation in the galaxies is being quickly quenched as they fall into the cluster. Similar behavior has been observed for low-redshift star forming galaxies (Mahajan et al. 2012).

Other than properties associated with star formation, no other property showed any strong indication of trends with radius.

5. The Fate of LCBGs in Clusters

In Crawford et al. (2014), we argued that cluster LCBGs are galaxies likely falling into the cluster for the first time based on their observed spatial and velocity distributions. In this work, we have shown that cluster LCBGs as a class are indistinguishable from field LCBGs in terms of dynamical mass, size, luminosity, metallicity, and star-formation rate. When combined with their relative absence from the cluster core, this further supports the idea that these galaxies are recent arrivals in the cluster environment.

Although some LCBGs may plausibly masquerade as low-surface-brightness disks with centrally-concentrated star formation (Barton & van Zee 2001), deep imaging of LCBGs has revealed that fewer than 10% of field sources exhibit any extended disk-like structure (Noeske et al. 2006; Barton et al. 2006). Regardless, any extended or low-surface-brightness structure

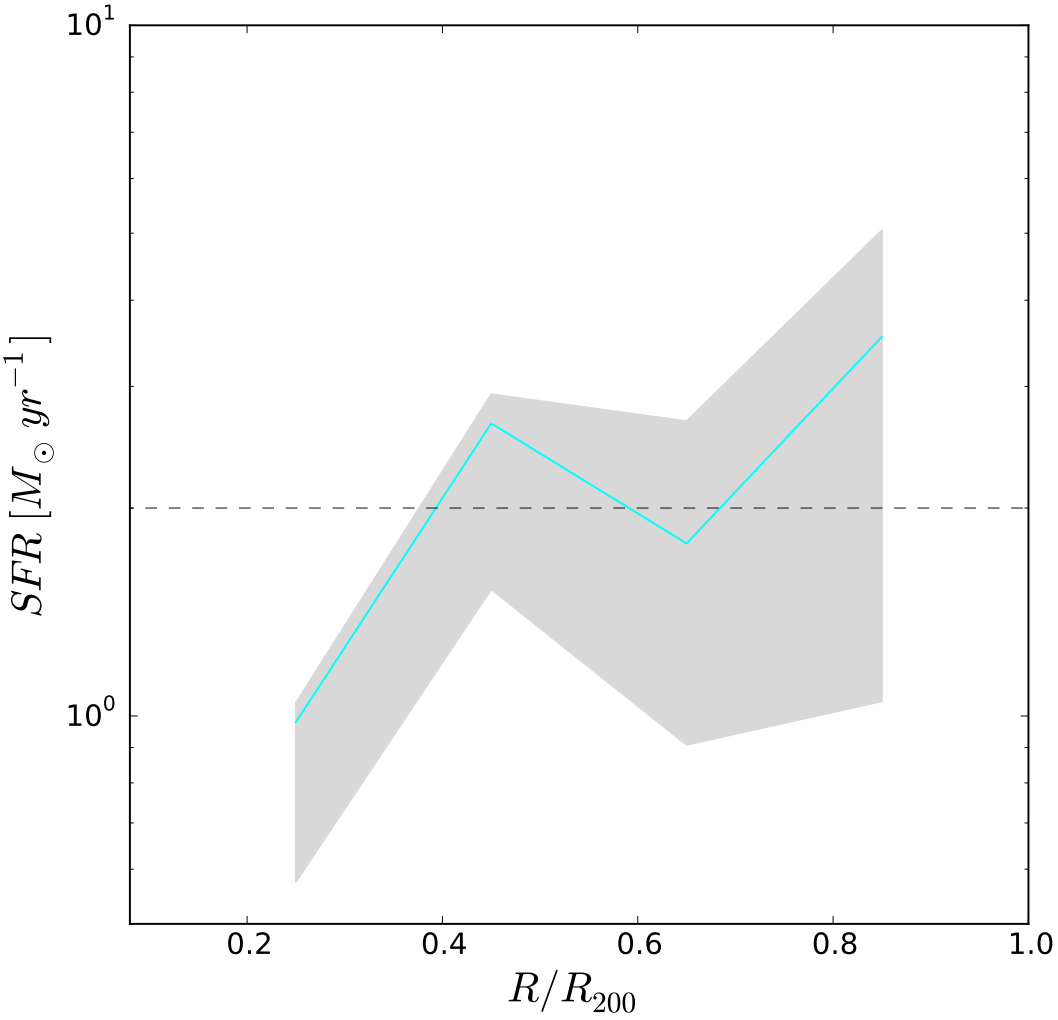

Fig. 5.— Mean star formation rate in LCBGs as a function of cluster radius. The cluster radius has been normalized by r_{200} for each cluster. The solid line indicates the mean while the gray area indicates the upper and lower quartiles. For comparison, we plot the average star formation rate for field LCBGs from our sample at $z = 0.7$ (black, dashed line) . The LCBGs show evidence for a rapid increase in star formation followed by a decline towards the cluster center.

will most likely be stripped away due to various cluster processes (Boselli & Gavazzi 2006). As such, the stars and gas that originally resided within LCBGs are likely to have either: 1) merged into other cluster galaxies, 2) dispersed to become part of the intracluster light (ICL), and/or 3) faded to become dwarf ellipticals. The following sections explore these three possible scenarios.

5.1. Merging of LCBGs

Based on our previous analysis of projected sky position and velocity relative to near neighbors, approximately 40% of LCBGs in clusters appear to be closely associated with another galaxy (Crawford et al. 2014). Previous observations of starburst galaxies in intermediate-redshift clusters also indicate a high percentage of interacting or merging systems (Couch et al. 1994; Moss 2006; Jaffé et al. 2011). Although the large velocity dispersion among cluster galaxies is expected to limit the number of mergers which can occur in the cluster core (Ghigna et al. 1998), galaxies falling in as part of groups may undergo mergers on the outskirts of clusters (Mihos 2003).

An open question is what will happen to these close associations of galaxies. After one passage through the cluster core, even small groups are likely to be tidally disrupted (Gonzalez-Casado et al. 1994). However, in their simulations Martel et al. (2012) find that most galaxies will end up merging with a larger galaxy over the lifetime of the cluster while many of the remaining galaxies will be tidally disrupted to become part of the ICL. By $z \sim 0.5$, most of the tidally disrupted material ends up being accreted onto larger galaxies. Detailed modeling of interactions between galaxy pairs in clusters is required to determine the fraction of LCBGs that will ultimately merge into other cluster galaxies.

However, we can estimate the number of mergers that are likely to occur from the velocities and positions of our LCBGs. For each LCBG, we plot in Figure 6 the projected distance and radial velocity difference between each LCBG and its nearest spectroscopic neighbor. From the simulations of Lotz et al. (2011) of the merger timescale for field galaxies at different separations, we estimate that pairs of galaxies with separations under 40 kpc are likely to merge within 1 Gyr–the typical crossing time for these clusters. After 1 Gyr, the pair would be expected to be separated by the cluster tidal forces. This distance is set as the maximum separation for galaxies likely to merge. The other limitation we place on the galaxies is that they should be gravitationally bound. The sloping line in Figure 6 defines the upper-limit of the region in the plot where objects are likely to be gravitationally bound to their companion, based on their distance and velocity difference if we assume that the companion has a typical mass of $M = 10^{11}\ M_{\odot}$. These two considerations allows us to define

an area in Figure 6 within which objects are likely to be mergers. Pairs that are near this threshold may still undergo a merger or experience tidal disruption, depending on their exact position and motion. Out of our sample, we estimate that 10% of sources will undergo a merger. This number may also be underestimated due to our spectroscopic incompleteness, as most of the LCBGs in our sample do not have any spectroscopic confirmation of their nearest projected neighbor's redshift. If we include all LCBGs with a bright companion ($R < 23$) within 40 kpc, we find that the merger rate could be as high as 35%.

5.2. Disruption of the LCBG Phase

Several processes serve as potential disruptors of LCBGs in the cluster environment. First, ram pressure stripping (Gunn & Gott 1972) may remove gas from the galaxies. Second, the high star-formation rates in LCBGs (relative to their dynamical masses) can eject a large amount of gas and dust via winds from star formation and supernovae. Third, tidal forces from gravitational interactions with neighboring galaxies or the overall cluster potential can also remove gas and stellar material from the galaxy (Moore et al. 1999).

The net result is that some combination of these three disruptive processes can potentially remove large fractions of the stars and gas from LCBGs. For example, simulations of just a "galaxy harassment" scenario by Moore et al. (1999) found that a typical high-surface-brightness galaxy[6] would lose 20% of its stellar mass over 5 Gyr in a cluster. For low surface-brightness galaxies, this percentage increases to 60%. The exact percentage of the stripping will depend on the orbital parameters, with closer approaches to the cluster center likely to result in greater mass loss (Moore et al. 1998). Low-mass galaxies are likely to be completely disrupted by tidal shocks (Gnedin 2003).

Furthermore, the high star-formation rate occurring in these systems is likely to further deplete their gas reservoirs. The timescale for gas depletion in local LCBGs was found to be on order of 100–200 Myr by Garland et al. (2005). If intermediate-redshift LCBGs have similar gas reservoirs, they would quickly exhaust their supply of gas at their observed star-formation rates without any need for stripping of the cold gas. Without the accretion of new gas, the transformation of LCBGs into dE galaxies could easily happen through the process of strangulation (Kawata & Mulchaey 2008). In addition, the on-going star formation is likely to drive strong galactic winds that could potentially deplete as much gas as the ongoing star formation (Bradshaw et al. 2013). If this gas is swept away by the ICM, it will further

[6]In Moore et al. (1999), high-surface-brightness galaxies were defined as having a luminosity of $\sim L^*$ and a disc scalelength of $r_d = 3kpc$. Low-surface-brightness galaxies have a disc scalelength of $r_d = 7kpc$.

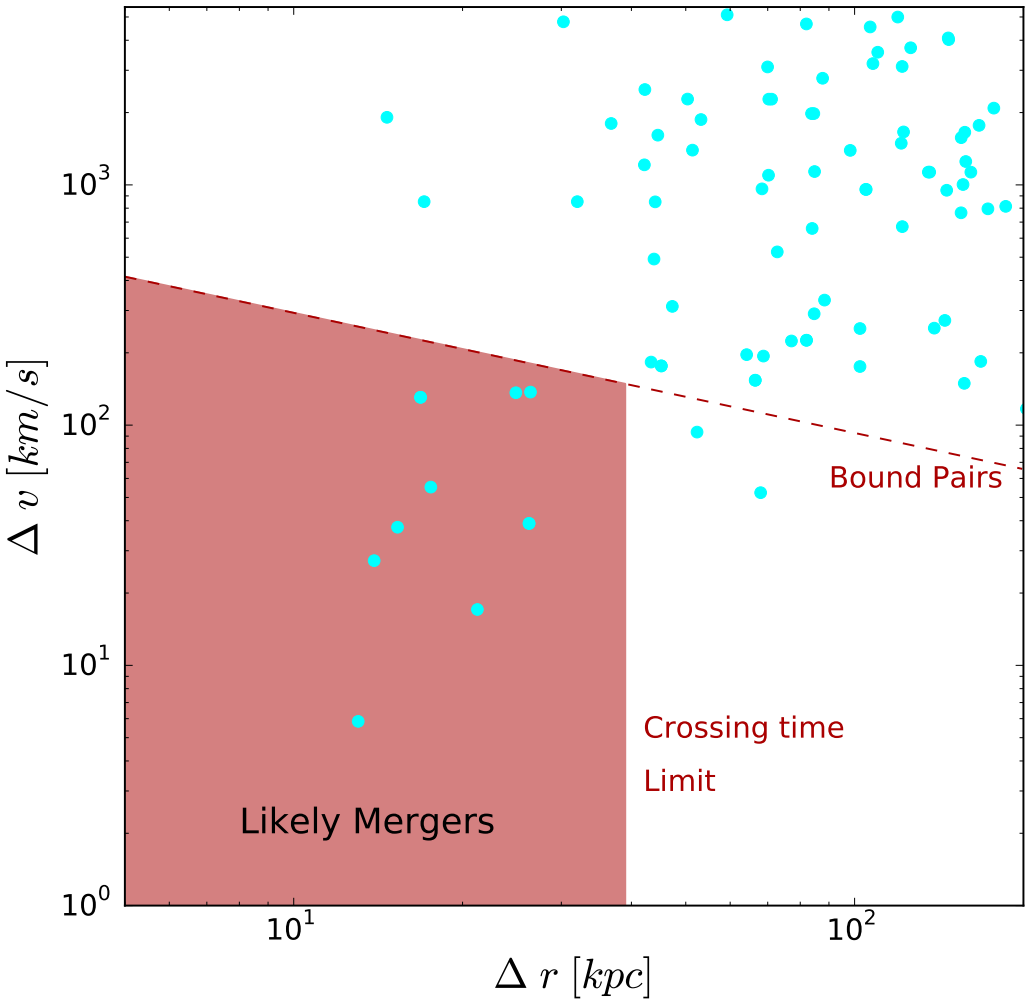

Fig. 6.— Velocity and projected distance of nearest spectroscopic neighbor for each LCBG. Objects within the pink shaded region are likely to form gravitationally-bound pairs that will merge. The right-hand limit to the plot is based on the typical timescale for mergers of field galaxies from Lotz et al. (2011) and the typical crossing time of the cluster, while the upper limit is based on the escape velocity from a $M = 10^{11}\ M_{\odot}$ companion. Based on confirmed pairs via spectroscopic , we estimate that 10% of LCBGs will undergo a merger with their companion.

hasten the quenching process. On the other hand, some of the material may remain in the LCBGs due to confinement from the hot intercluster medium (Murakami & Babul 1999).

Due to the available gas, high star formation rates, and extreme cluster environments, LCBGs will likely be quenched on very short time scales. Once star formation ceases, the galaxy is likely to rapidly fade and redden to move out of the LCBG phase (Koo et al. 1995).

5.3. LCBGs as Progenitors of Dwarf Ellipticals

Regardless of what happens to the stripped stars and gas, LCBGs have long been proposed as the progenitors of lower-mass galaxies once their current burst of star formation has faded (Guzman et al. 1996; Koo et al. 1997). The local-group, dE galaxy NGC 205 is often cited as a possible descendant of LCBGs. NCG 205 has a velocity dispersion of 42 km s^{-1}, an effective radius of 2.5 kpc, and an absolute magnitude of $M_B = -15.0$ (Geha et al. 2006). In addition, the metallicity of NGC 205 as measured from planetary nebulae is $12 + \log(\mathrm{O/H}) = 8.6$ (Richer & McCall 1995). This is very comparable to our sample of cluster objects which have a median velocity dispersion of 56 km s^{-1}, a size of 1.8 kpc, and a $12 + \log(\mathrm{O/H}) = 8.6$. The median absolute magnitude is $M_B = -19.9$ for cluster LCBGs, which would represent fading of up to 4.9 mag. The ultimate luminosity of a post-starburst system will depend on any underlying stellar population, the strength of the current burst, and whether the galaxy is quenched. For a single stellar population, the expected fading is 5–7 mag after 5-9 Gyrs based on the models from Bruzual & Charlot (2003). For comparison, a model with an exponential-declining star formation with e-folding time of 1 Gyr followed by a 100 Myr burst that occurs 5 Gyrs after the galaxy formed and is equal to 10% of the current stellar mass would be expected to fade between 2.5–3 mags over the same period of time. Depending on how extreme these starburst events are, it would be reasonable to assume that a typical LCBG could end up as perhaps a slightly smaller version of NGC 205 once star formation terminates.

One longstanding criticism of the hypothesis that LCBGs evolve into dE is that the gas phase metallicity of the LCBGs was too high for the average stellar populations found in NGC 205 (Kobulnicky & Zaritsky 1999) as measured by oxygen abundances in planetary nebulae. Yet, a range of values are found within the planetary nebulae in NGC 205 (Gonçalves et al. 2014), and the more appropriate comparison would be with the most metal rich planetary nebula in a galaxy, which would reflect the gas phase metallicity of the last star formation event rather than the average over the history of star formation in the galaxy. Furthermore, typical dE galaxies in the Virgo cluster have α-element metallicities exhibiting a large scatter around solar (Michielsen et al. 2008), which is close to what we measure for

the intermediate-redshift LCBGs.

Furthermore, dE galaxies in low redshift clusters show a range of star-formation histories (Conselice et al. 2003; Michielsen et al. 2008; Koleva et al. 2009; Paudel et al. 2010) and accretion histories (Conselice et al. 2001; Smith et al. 2012). Penny et al. (2014) find that dE in Perseus formed from disk galaxies stripped through harassment and Michielsen et al. (2008) find that star formation in the dE population in Virgo likely was truncated as the galaxies were accreted into the cluster over time. Lisker (2009) reports that present-epoch dE galaxies form a morphologically diverse group with $\sim$ 50% having a strong nucleus, 20% having a disk, and 10% having a blue core. Along with the different morphologies, the different types are shown to have a range of stellar ages and distributions within the clusters. A single evolutionary path is unlikely, but an important next step will be to look at the individual morphologies of LCBGs and to simulate how they will evolve in the cluster environment.

Even though LCBGs form a relatively homogeneous class in these distant clusters of galaxies, their differing infall trajectories will result in different processes affecting their subsequent evolution after entering the cluster. Not only will the cluster environment strip material from the LCBGs, it will also transform them. Aguerri & González-García (2009) show that fast tidal interactions are very efficient at stripping the outer parts of galaxies and that bright, late-type galaxies could easily be transformed into early-type dwarf galaxies by removing any outer halo or disk of the galaxies. As dense systems are likely to be least disrupted (Moore et al. 1998), LCBGs with concentrated star formation are the most likely to survive in the cluster environment. Hence, these initially similar galaxies may evolve into a diversity of morphological types today. Detailed modeling of each of these galaxies may help to connect them to their eventual dE counterparts.

5.4. Number density evolution of LCBGs

To calculate the number of descendants of LCBGs in present-day galaxy clusters, we make the following assumptions about how they will evolve and what their properties are:

- 10% of the LCBG sample will merge with other cluster galaxies as measured from our sample.
- The stellar-mass-to-dynamical-mass ratio for LCBGs is 0.4 as measured by Guzmán et al. (2003).
- The star formation of an LCBG is quenched immediately upon entering the cluster.

- The amount of fading will be given by a Bruzual & Charlot (2003) model that had a star formation history characterized by declining star formation followed by a starburst equal to 10% of its stellar mass that occurs when the galaxy is accreted onto the cluster.
- $20 - 60\%$ of the stellar mass will be stripped during each passage through the cluster.
- The accretion rate of LCBGs at a given redshift will be given by the cluster luminosity function at that redshift divided by the visibility period for LCBGs.
- The cluster luminosity function of LCBGs evolves linearly between those measured above between z=0.5-0.9 to z=0, where it is assumed to have a value of zero.
- The LCBG phase is visible for between 200-600 Myrs.

The final item is based on the expected lifetime for LCBGs. If their star formation were immediately quenched, LCBGs would redden over time so that the typical LCBGs in our sample would no longer meet the established color criterion within 400 Myr. At these redshifts and cluster masses, the SFR peaks at a radius of 1 Mpc from the cluster core and almost no star formation is seen within 0.25 Mpc of the cluster core. A typical object within the cluster would take 600 Myr to cross this distance. Accordingly, we take this as the upper limit for the visibility time for an LCBG. For a lower limit, we use the estimate of 200 Myr from Garland et al. (2005) based on the amount of time it would take for the LCBGs to exhaust their gas reservoir.

Based on our sample, we can calculate the evolution in the cluster luminosity function. Figure 7 compares the $0.7 < z < 0.9$ and $z = 0.55$ luminosity functions of cluster LCBGs. The luminosity functions were calculated by summing over all LCBGs in the cluster within R_{200} and correcting for spectroscopic incompleteness in the same manner as in Crawford et al. (2011). The luminosity function for each cluster was then normalized by the volume of the cluster as estimated from the R_{200} values given in Table 1 of Crawford et al. (2014). Finally, we averaged the luminosity functions into the two redshift bins. For reference, the average volume of our z=0.55 (z=0.83) redshift clusters is 74 Mpc^3 (16 Mpc^3). The values for the observed luminosity functions are given in Table 3. For both luminosity functions, we have fit Schechter functions with a fixed slope of $\alpha = 1.1$. At $z = 0.55$, the luminosity function has a value of $M_B = -21.30$ and $\phi_* = 0.217$ galaxies/Mpc^3; at $z = 0.83$, $M_B = -21.97$ and $\phi_* = 0.92$ galaxies/Mpc^3. As can be seen, the number density and luminosity of LCBGs rapidly evolve between $z = 0.83$ and $z = 0.55$, an effect reported previously (Phillips et al. 1997; Crawford et al. 2011).

Using the observed evolution in the LCBG luminosity function, we simulate a cluster accreting LCBGs between $z = 1.0$ and $z = 0.0$. Once an LCBG is accreted, it evolves based

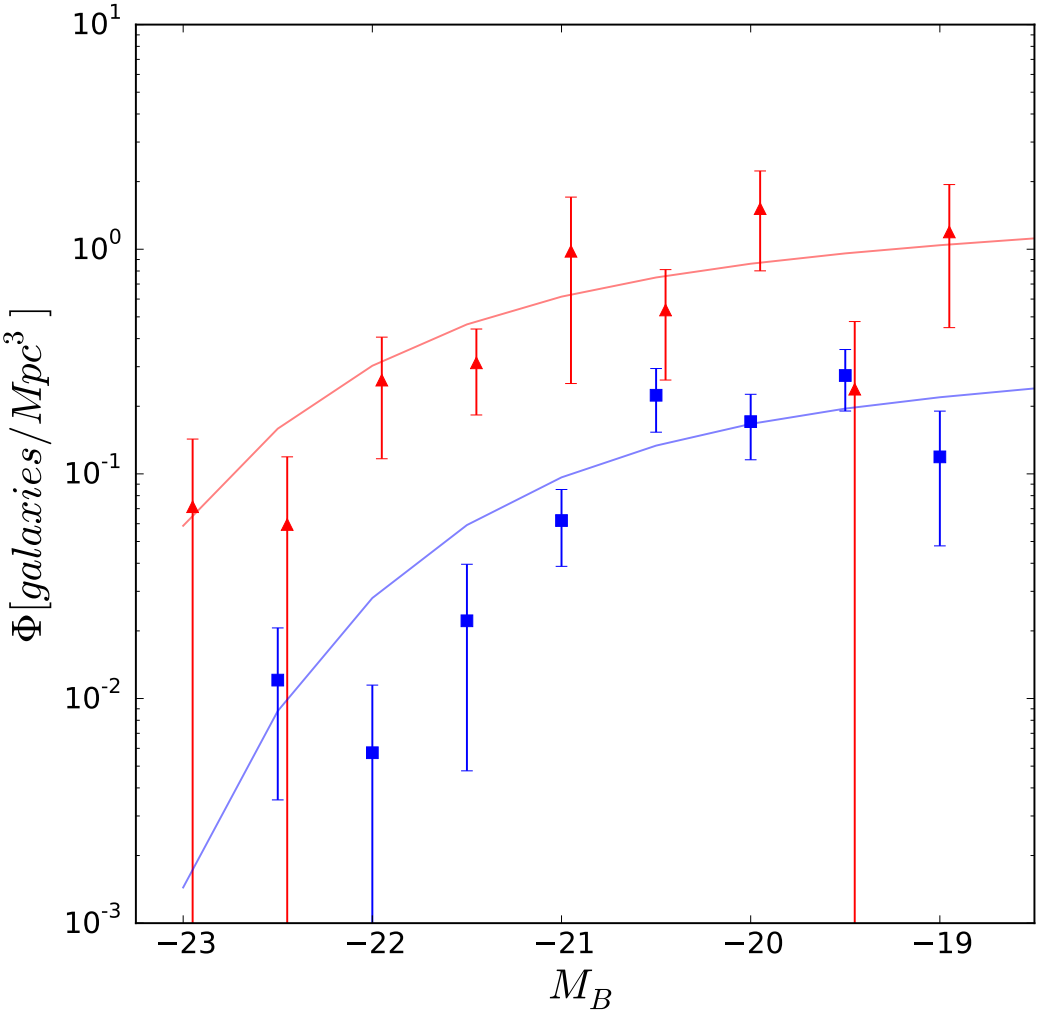

Fig. 7.— The $z = 0.55$ (blue squares) and $z = 0.83$ (red triangles) luminosity functions for LCBGs. To both luminosity functions, we have fit Schechter functions with a fixed slope of $\alpha = 1.1$. The cluster LCBG functions show the similar decrease in number density as seen in the field. The z=0.83 luminosity function has been offset by 0.05 mag for clarity.

on the assumptions outlined above. The resulting luminosity functions for these sources are presented as the red region in Figure 8. Overall, the accretion of LCBGs into galaxy clusters would result between 600–1800 objects with $M_B < -10$ being added to the cluster. These numbers are similar to the number of dE found in low-redshift clusters (Ferguson & Sandage 1988; Secker et al. 1997). For comparison, we plot the luminosity function for dEs in the Fornax Cluster from Ferguson & Sandage (1988) and Coma Cluster from Thompson & Gregory (1993). We have normalized both luminosity functions to the expected $z = 0$ mass (4.9×10^{15} $M_\odot$) of our intermediate-redshift cluster based on the predictions from Wechsler et al. (2002) and corrected the area of the original surveys to a value of R_{200}.

For the assumptions outlined above, we estimate that LCBGs accreted between z=1.0 and 0 account for 38% of dE galaxies brighter than $M_B < -14.5$. Changes to the assumptions about the stripping in galaxies will result in a maximum change of 10% in the fraction of dE descendants. An increase (decrease) in the amount of fading by 1 mag will change the percentage of dEs to 23% (50%). Finally, the largest effect on the percentage of bright dEs is the visibility of the LCBG phase. For the shorter period of 200 Myr, LCBGs could account for up to 77% of dEs; for 600 Myrs, LCBGs would only account of 25% of dEs.

The fraction of dE galaxies in present-day clusters which were once LCBGs remains uncertain. The simple assumptions made about their evolution do not match in detail the shape of the observed low redshift luminosity functions of dwarf ellipticals as can be seen in Figure 8. However, even at the lowest estimates, a significant fraction of dEs in local clusters would have gone through an LCBG phase at intermediate redshifts. Better limits on how these galaxies have evolved require more detailed investigation of the evolution of individual galaxies, taking a holistic look at the properties of local dE galaxies, and improving measurements of their luminosity functions.

Table 3. LCBG Luminosity Functions

M_B	ϕ at z=0.55 galaxies/Mpc^3	ϕ at z=0.83 galaxies/Mpc^3
-23.00	0.000 ± 0.000	0.071 ± 0.071
-22.50	0.012 ± 0.009	0.060 ± 0.060
-22.00	0.006 ± 0.006	0.486 ± 0.243
-21.50	0.022 ± 0.017	0.427 ± 0.180
-21.00	0.062 ± 0.023	1.013 ± 0.463
-20.50	0.224 ± 0.071	0.611 ± 0.327
-20.00	0.171 ± 0.055	1.256 ± 0.452
-19.50	0.274 ± 0.084	0.092 ± 0.092
-19.00	0.119 ± 0.071	1.230 ± 0.541

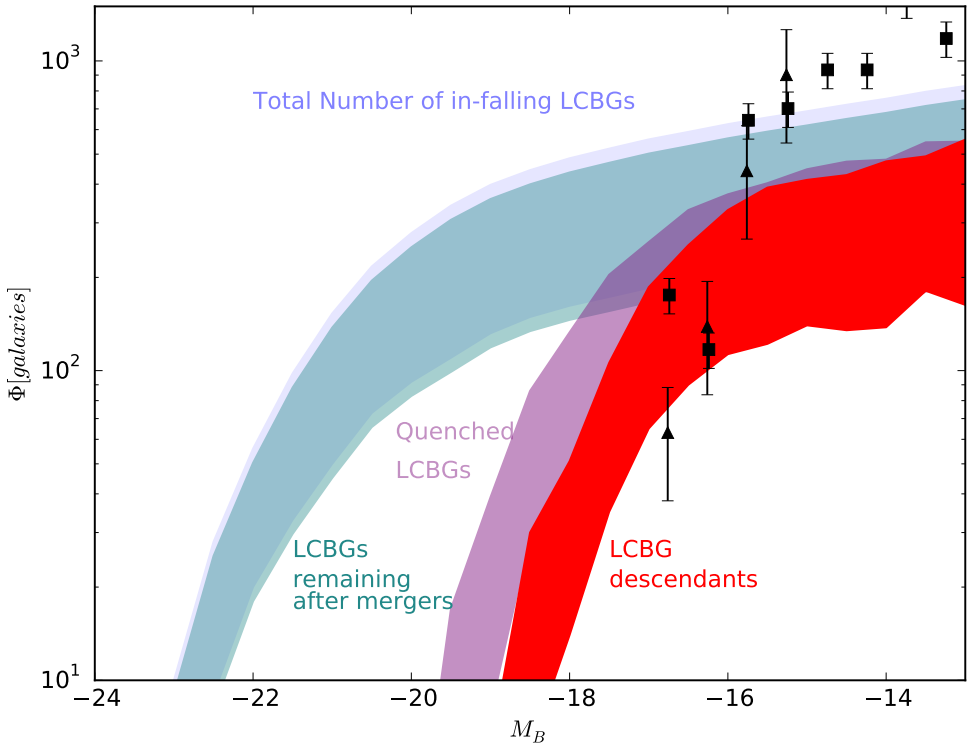

Fig. 8.— Predicted evolution of the number density of LCBGs in a massive galaxy cluster. The gray curve represents the total number of LCBGs accreted onto the cluster since $z = 1.0$. The width of the curve represents two assumptions about the amount of time the LCBG phase is visible, with the upper limit representing a visibility window of 200 Myr and the lower limit corresponding to 600 Myr. The teal curve represents the number of LCBGs remaining after 10% of LCBGs merge with other galaxies. The purple curve represents the distribution of LCBGs after their star formation is quenched and they begin to fade. The descendants of LCBGs – after accounting for mergers, fading, and stripping from the cluster environment – lie within the red region. For comparison, the luminosity function for dwarf elliptical galaxies in Fornax from Ferguson & Sandage (1988) and Coma from Thompson & Gregory (1993) normalized to the mass and area of our clusters at $z = 0$ is plotted as black squares and triangles, respectively. It is likely that approximately $50 \pm 20\%$ of dE galaxies seen in present day clusters underwent an LCBG phase since $z = 1$.

6. Conclusion

In this work, we have reported on the rest-frame properties of LCBGs, an extreme star-bursting population seen at intermediate redshifts. Based on ground- and space-based imaging and spectroscopy, we have measured the size, luminosity, star-formation rate, metallicity, and dynamical mass of the LCBGs. Based on these measurements, we have observed:

1. Much of the evolution in the size-luminosity relationship for blue cluster galaxies appears to be driven by the inclusion of LCBGs at intermediate redshift. No evolution is observed in this relationship if LCBGs are excluded from the fit.

2. We detect no significant differences in the size, mass, luminosity, star formation rate or metallicity of field and cluster LCBGs. To the degree we can discern, all of the key characteristics appear similar between the two populations.

3. 35% of cluster LCBGs show evidence for obscured star formation with no strong trends found with either LCBG properties or cluster position.

4. The star-formation rate of cluster LCBGs decreases towards the core of the cluster. Almost no LCBGs are observed in the core of these clusters and the star formation appears to peak beyond $0.5R_{200}$.

5. Of the LCBGs currently falling into the cluster, 10% are likely to merge with a nearby neighbor as they pass through the cluster.

6. The size, mass, and metallicity of LCBGs at intermediate redshift are very similar to the properties of present-day dwarf elliptical galaxies. Galaxy evolution models predict that if their star formation were quenched, the LCBG population would evolve in magnitude and color so as to produce galaxies that closely resemble today's dwarf elliptical population.

7. Based on assumptions about their evolution and accretion rate, LCBGs seen at intermediate redshifts ($z < 1$) could account for 30–75% of all dwarf ellipticals seen in clusters today.

An important next step will be to trace the evolution of these sources through realistic simulations of the cluster environment accounting for the physics of both the stellar and gas components of these galaxies. As the distribution and properties of the LCBG population matches the population of dwarf elliptical galaxies in clusters, it will be important to determine which physical interactions with the cluster environment are the predominant

mechanisms in transforming LCBGs into dwarf elliptical galaxies. Exploring how the LCBG population fits into the evolution of other cluster populations and how the overall cluster population changes with time will be critical to understanding the transformation of galaxies in clusters.

We thank the referee for the careful reading of our manuscript and the constructive criticism that improved our paper. S.M.C. acknowledges the South African Astronomical Observatory and the National Research Foundation of South Africa for support during this project. M.A.B. acknowledges support from NSF grant AST-1009471.

This research made use of Astropy, a community-developed core Python package for Astronomy (Astropy Collaboration et al. 2013). This research has made use of the NASA/IPAC Extragalactic Database (NED) and NASA/IPAC Infrared Science Archive which are operated by the Jet Propulsion Laboratory, California Institute of Technology, under contract with the National Aeronautics and Space Administration.

Based on observations made with the NASA/ESA Hubble Space Telescope, obtained from the data archive at the Space Telescope Science Institute. STScI is operated by the Association of Universities for Research in Astronomy, Inc. under NASA contract NAS 5-26555.

The WIYN Observatory is a joint facility of the University of Wisconsin-Madison, Indiana University, the National Optical Astronomy Observatory and the University of Missouri.

Our findings are based on observations acquired at the W. M. Keck Observatory, which operates as a scientific partnership among the California Institute of Technology, the University of California and the National Aeronautics and Space Administration. The generous financial support of the W. M. Keck Foundation made the Observatory possible.

The authors wish to recognize and acknowledge the very significant cultural role and reverence that the summit of Maunakea has always had within the indigenous Hawaiian community. We consider ourselves fortunate to have had the opportunity to conduct observations from this mountain.

Facilities: WMKO, WIYN

REFERENCES

Aguerri, J. A. L., & González-García, A. C. 2009, A&A, 494, 891

Alonso-Herrero, A., Aragón-Salamanca, A., Zamorano, J., & Rego, M. 1996, MNRAS, 278, 417

Astropy Collaboration, Robitaille, T. P., Tollerud, E. J., et al. 2013, A&A, 558, A33

Balogh, M. L., Couch, W. J., Smail, I., Bower, R. G., & Glazebrook, K. 2002, MNRAS, 335, 10

Bamford, S. P., Milvang-Jensen, B., & Aragón-Salamanca, A. 2007, MNRAS, 378, L6

Barton, E. J., & van Zee, L. 2001, ApJ, 550, L35

Barton, E. J., van Zee, L., & Bershady, M. A. 2006, ApJ, 649, 129

Bershady, M. A., Jangren, A., & Conselice, C. J. 2000, AJ, 119, 2645

Biviano, A., Katgert, P., Mazure, A., et al. 1997, A&A, 321, 84

Boselli, A., & Gavazzi, G. 2006, PASP, 118, 517

Bradshaw, E. J., Almaini, O., Hartley, W. G., et al. 2013, MNRAS, 433, 194

Bretherton, C. F., James, P. A., Moss, C., & Whittle, M. 2010, A&A, 524, A24

Bruzual, G., & Charlot, S. 2003, MNRAS, 344, 1000

Butcher, H., & Oemler, Jr., A. 1984, ApJ, 285, 426

Conselice, C. J., Gallagher, III, J. S., & Wyse, R. F. G. 2001, ApJ, 559, 791

—. 2003, AJ, 125, 66

Couch, W. J., Ellis, R. S., Sharples, R. M., & Smail, I. 1994, ApJ, 430, 121

Crawford, S. M., Bershady, M. A., Glenn, A. D., & Hoessel, J. G. 2006, ApJ, 636, L13

Crawford, S. M., Bershady, M. A., & Hoessel, J. G. 2009, ApJ, 690, 1158

Crawford, S. M., Wirth, G. D., & Bershady, M. A. 2014, ApJ, 786, 30

Crawford, S. M., Wirth, G. D., Bershady, M. A., & Hon, K. 2011, ApJ, 741, 98

Domínguez Sánchez, H., Mignoli, M., Pozzi, F., et al. 2012, MNRAS, 426, 330

Ellis, R. S. 1997, ARA&A, 35, 389

Faber, S. M., Phillips, A. C., Kibrick, R. I., et al. 2003, in Society of Photo-Optical Instrumentation Engineers (SPIE) Conference Series, Vol. 4841, Instrument Design and Performance for Optical/Infrared Ground-based Telescopes, ed. M. Iye & A. F. M. Moorwood, 1657–1669

Ferguson, H. C., & Sandage, A. 1988, AJ, 96, 1520

Finn, R. A., Zaritsky, D., McCarthy, Jr., D. W., et al. 2005, ApJ, 630, 206

Garland, C. A., Pisano, D. J., Williams, J. P., Guzmán, R., & Castander, F. J. 2004, ApJ, 615, 689

Garland, C. A., Williams, J. P., Pisano, D. J., et al. 2005, ApJ, 624, 714

Geha, M., Guhathakurta, P., Rich, R. M., & Cooper, M. C. 2006, AJ, 131, 332

Ghigna, S., Moore, B., Governato, F., et al. 1998, MNRAS, 300, 146

Gnedin, O. Y. 2003, ApJ, 589, 752

Gómez, P. L., Nichol, R. C., Miller, C. J., et al. 2003, ApJ, 584, 210

Gonçalves, D. R., Magrini, L., Teodorescu, A. M., & Carneiro, C. M. 2014, MNRAS, 444, 1705

Gonzalez-Casado, G., Mamon, G. A., & Salvador-Sole, E. 1994, ApJ, 433, L61

Gunn, J. E., & Gott, III, J. R. 1972, ApJ, 176, 1

Guzmán, R., Gallego, J., Koo, D. C., et al. 1997, ApJ, 489, 559

Guzman, R., Koo, D. C., Faber, S. M., et al. 1996, ApJ, 460, L5

Guzmán, R., Östlin, G., Kunth, D., et al. 2003, ApJ, 586, L45

Hammer, F., Gruel, N., Thuan, T. X., Flores, H., & Infante, L. 2001, ApJ, 550, 570

Hoyos, C., Guzmán, R., Díaz, A. I., Koo, D. C., & Bershady, M. A. 2007, AJ, 134, 2455

Jaffé, Y. L., Aragón-Salamanca, A., Kuntschner, H., et al. 2011, MNRAS, 417, 1996

Kawata, D., & Mulchaey, J. S. 2008, ApJ, 672, L103

Kennicutt, Jr., R. C. 1992, ApJ, 388, 310

Kent, S. M. 1984, ApJS, 56, 105

Kobulnicky, H. A., & Kewley, L. J. 2004, ApJ, 617, 240

Kobulnicky, H. A., & Zaritsky, D. 1999, ApJ, 511, 118

Koleva, M., de Rijcke, S., Prugniel, P., Zeilinger, W. W., & Michielsen, D. 2009, MNRAS, 396, 2133

Koo, D. C., Bershady, M. A., Wirth, G. D., Stanford, S. A., & Majewski, S. R. 1994, ApJ, 427, L9

Koo, D. C., Guzman, R., Faber, S. M., et al. 1995, ApJ, 440, L49

Koo, D. C., Guzmán, R., Gallego, J., & Wirth, G. D. 1997, ApJ, 478, L49

Lisker, T. 2009, Astronomische Nachrichten, 330, 1043

Lotz, J. M., Jonsson, P., Cox, T. J., et al. 2011, ApJ, 742, 103

Mahajan, S., Raychaudhury, S., & Pimbblet, K. A. 2012, MNRAS, 427, 1252

Martel, H., Barai, P., & Brito, W. 2012, ApJ, 757, 48

McMaster, M., Biretta, J., & et al. 2008, Wide Field and Planetary Camera 2 Instrument Handbook (Baltimore: STScI)

Michielsen, D., Boselli, A., Conselice, C. J., et al. 2008, MNRAS, 385, 1374

Mihos, C. 2003, ArXiv Astrophysics e-prints, astro-ph/0305512

Moore, B., Lake, G., & Katz, N. 1998, ApJ, 495, 139

Moore, B., Lake, G., Quinn, T., & Stadel, J. 1999, MNRAS, 304, 465

Moss, C. 2006, MNRAS, 373, 167

Murakami, I., & Babul, A. 1999, MNRAS, 309, 161

Noeske, K. G., Koo, D. C., Phillips, A. C., et al. 2006, ApJ, 640, L143

Pagel, B. E. J., Edmunds, M. G., Blackwell, D. E., Chun, M. S., & Smith, G. 1979, MNRAS, 189, 95

Paudel, S., Lisker, T., Kuntschner, H., Grebel, E. K., & Glatt, K. 2010, MNRAS, 405, 800

Penny, S. J., Forbes, D. A., Pimbblet, K. A., & Floyd, D. J. E. 2014, MNRAS, 443, 3381

Phillips, A. C., Guzmán, R., Gallego, J., et al. 1997, ApJ, 489, 543

Randriamampandry, S. M., Crawford, S. M., Cress, C. M., et al. 2015, MNRAS, 447, 168

Rawat, A., Kembhavi, A. K., Hammer, F., Flores, H., & Barway, S. 2007, A&A, 469, 483

Richer, M. G., & McCall, M. L. 1995, ApJ, 445, 642

Rieke, G. H., Alonso-Herrero, A., Weiner, B. J., et al. 2009, ApJ, 692, 556

Secker, J., Harris, W. E., & Plummer, J. D. 1997, PASP, 109, 1377

Smith, R. J., Lucey, J. R., Price, J., Hudson, M. J., & Phillipps, S. 2012, MNRAS, 419, 3167

Thompson, L. A., & Gregory, S. A. 1993, AJ, 106, 2197

Tollerud, E. J., Barton, E. J., van Zee, L., & Cooke, J. 2010, ApJ, 708, 1076

Tran, K.-V. H., van Dokkum, P., Illingworth, G. D., et al. 2005, ApJ, 619, 134

Ubeda, L., , & et al. 2014, ACS Instrument Handbook (Baltimore: STScI)

Wechsler, R. H., Bullock, J. S., Primack, J. R., Kravtsov, A. V., & Dekel, A. 2002, ApJ, 568, 52

Werk, J. K., Jangren, A., & Salzer, J. J. 2004, ApJ, 617, 1004

Willmer, C. N. A., Faber, S. M., Koo, D. C., et al. 2006, ApJ, 647, 853

This preprint was prepared with the AAS LaTeX macros v5.2.